Politecnico di Torino

Politecnico di Torino

Sustainable Nuclear Energy

2024/2025

Graduation Session November 2025

Mechanical and electrical characterization of composite conductors based on High-Temperature Superconducting tapes for fusion applications

Supervisors:

Monica Ferraris

Emeric Benoist

Gilles Lenoir

Candidate:

Andrea De Marco

Abstract

This report presents the work carried out during an internship at CEA, within the framework of the PEPR Suprafusion project, which aims to develop technologies for nuclear fusion applications.

The study focuses on the mechanical and electrical characterization of composite conductors based on High-Temperature Superconducting (HTS) tapes developed at CEA.

The first part of the work involved analyzing the parameters and methodologies of the assembly process. Critical aspects were identified and addressed to improve both efficiency and reproducibility. In addition, metallographic analyses were performed on conductor cross-sections to better evaluate the geometry of the HTS tape and the quality of the brazing process.

The second part of the work focused on the electrical characterization of the conductor through liquid nitrogen testing, with the objective of determining its critical current. A dedicated procedure was developed for data acquisition and analysis.

Subsequently, mechanical characterization was carried out through tensile, compression, bending, and torsion tests to evaluate the conductor's behavior under applied stress and to determine its mechanical properties. After each mechanical test, new electrical measurements were performed to assess any degradation in the critical current. This approach allowed the identification of stress and strain thresholds beyond which the superconductor's performance is compromised.

Finally, a dedicated section investigates the stresses experienced by the HTS tape within the conductor during the heat treatment of the assembly process and the thermal contraction occurring under cryogenic conditions in liquid nitrogen.

Table of Contents

List of Figures

Chapter 1

Introduction

The **CEA** (Commissariat à l'énergie atomique et aux énergies alternatives) is a leading French public research organization recognized for its work in energy, defense, and advanced technologies. Within the CEA, the **IRFU** (Institute of Research into the Fundamental Laws of the Universe), based at Paris-Saclay, combines fundamental research in fields such as astrophysics, nuclear and particle physics with the development of advanced instrumentation, including accelerators, superconducting magnets, and complex electronic systems[1].

This internship, entitled "Mechanical and electrical characterization of composite conductors based on High-Temperature Superconducting tapes for fusion applications", focused on the development of HTS-based composite conductors from assembly to final testing as part of one of the objectives of the PEPR Suprafusion project in which the CEA is one of the contributors.
The objective was to study how the design and process parameters influence the mechanical and electrical behavior of the conductors, with the aim of optimizing their performance in high-field superconducting magnets.

High-Temperature Superconductors (HTS) are key to enabling compact and efficient magnetic confinement systems in future fusion reactors, a central part of the global transition to sustainable, low-carbon energy[2]. The research conducted at CEA contributes to overcoming the main technological challenges in this field, particularly through the development and characterization of advanced superconducting conductors.

This report presents the work carried out during the internship, outlining the institutional framework, the technical procedures implemented, and the key results obtained, with the aim of contributing to future developments in HTS conductor technology for fusion applications.

The report is organized as follows: the first section introduces the scientific and technological context of the PEPR Suprafusion project and the role of High-Temperature Superconductors in fusion research; the second section presents the analysis of the conductor assembly process and the improvements proposed; the third section describes the electrical testing procedures and results; the fourth section focuses on the mechanical characterization of the conductor and its correlation with electrical degradation following mechanical stress.

Chapter 2

Context

2.1 The PEPR Suprafusion Project

The PEPR (Plan Européen de Recherche et d'Innovation) is an initiative launched by the French government to support and coordinate research and innovation in strategic sectors such as energy, health, and digital technologies. The plan aims to strengthen France's position in scientific and technological innovation while addressing global challenges.

The focus of the **PEPR Suprafusion** program is on the development of advanced technologies for nuclear fusion, a promising field for the future of clean energy. The main objective is to accelerate research and development of materials and systems necessary for the design of efficient fusion reactors. Among the key technologies supported by PEPR Suprafusion are **High-Temperature Superconductors** (HTS), which are essential for generating the strong magnetic fields needed to confine plasma in compact fusion devices.

The program, co-led by CEA-Irfu and CNRS Ingénierie, is funded with 50 million euros over six years. To achieve its goals, it is structured around three main pillars[3]:

1. Development of the technological building blocks for HTS materials;
2. Demonstration of large-scale technological reliability;
3. Exploration of innovative applications.

A key milestone is the development of a 10 kA-class conductor based on HTS tapes, intended for the construction of a prototype solenoid to evaluate this technology.

The program aims to address the major technological challenges related to the design and fabrication of large-scale HTS magnets, characterized by substantial

dimensions (approximately 2 m × 3 m), very high operating currents, and intense magnetic fields (up to 20 T on the conductor). The magnetic energy stored in these systems reaches up to 100 MJ, emphasizing the importance of developing robust and reliable conductors[4].

The "R&D conducteur" work package focuses on the development of a composite conductor concept made of two 12 mm wide superconducting tapes, soldered together with copper lamination on both sides.

The goals of the research group include:

- Developing and studying soldering processes specific to this conductor type, considering parameters such as solder alloy, flux, and temperature control;
- Qualifying the performance degradation at each manufacturing step, including single tape, double tape soldering, tinning, soldering, copper lamination, bending, and junctions;
- Characterizing the mechanical and electrical properties of the conductor under operating conditions;
- Producing several 3-meter-long conductor samples for initial quench studies.

The final key objective of the research group is to study and **validate a scalable in-line production concept**. The aim is to develop a process that enables rapid and low-cost production of conductor lengths ranging from 10 to 200 meters, required for the fabrication of second-generation prototypes.

In parallel, other research groups are working on additional aspects of the demonstrator design, such as protection systems for the conductor and the development of test infrastructure. This collaborative effort ensures that all critical components of the fusion magnet system are addressed, from materials to integration and testing[4].

2.2 HTS characteristics

Superconductivity is a quantum state of matter characterized by zero electrical resistance and the expulsion of magnetic fields when a material is cooled below a certain critical temperature T_c.
According to this criterion, superconductors can be classified as:

- Low Temperature Superconductors (LTS), with a critical temperature below 40 K.
- High Temperature Superconductors (HTS), with a critical temperature above 40 K.

The superconducting state of a material is governed by three interdependent critical parameters:

- The **critical temperature** T_c is the maximum temperature below which a material exhibits superconductivity. Above this temperature, the material returns to a normal resistive state.
- The **critical magnetic field** B_c is the highest magnetic field strength a superconductor can withstand while remaining in the superconducting state. Beyond this field, superconductivity is destroyed.
- The **critical current density** J_c is the maximum electric current per unit area that the superconductor can carry without losing its superconducting properties. Exceeding this current generates magnetic fields that can disrupt the superconducting state.

Exceeding any of these thresholds results in the breakdown of the superconducting state and a return to normal resistive behavior. These limits define the operational boundaries for the use of superconductors in practical applications. Each superconductor has its own critical values, which can be represented in a three-dimensional graph called a critical surface. Superconductivity is sustained only within this volume, as shown in the figure below.

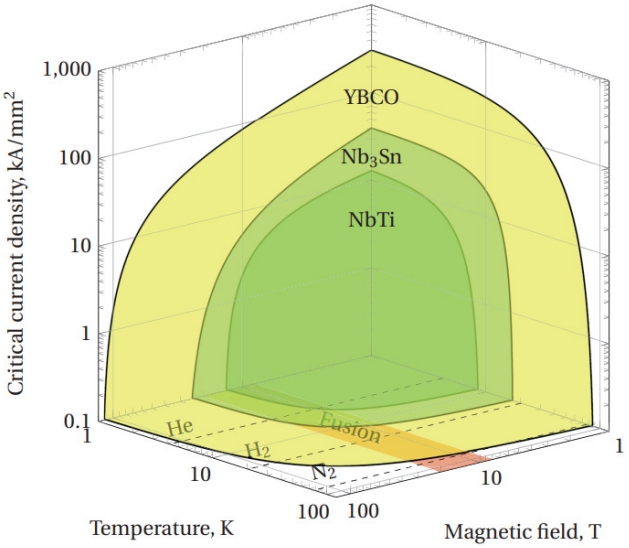

Figure 2.1: Critical current density as a function of magnetic field and temperature for YBCO (HTS), Nb_3Sn and NbTi (LTS). The critical surfaces show the parameter space in which the material remains superconducting[5].

HTS materials are promising for constructing electromagnets with high magnetic induction (>20 T). These materials are widely considered in high-energy physics, particularly for fusion applications.
Compared to Low-Temperature Superconductors (LTS) like NbTi and Nb_3Sn, HTS materials offer several advantages. Notably, they exhibit a lower dependence of J_c on temperature in the 5 K range, allowing operation closer to J_c while maintaining an adequate thermal margin. Additionally, they have much better thermal stability, requiring significantly more energy to trigger a quench, making HTS more robust against thermal disturbances.

However, in the event of a quench, they exhibits slow propagation of the hot zone and a gradual voltage rise. This can delay fault detection and cause localized overheating. Therefore, HTS conductors must be equipped with appropriate stabilizing layers to increase thermal capacity and electrical conductivity.

From a mechanical standpoint, the tapes exhibit a high axial stress limit (above 700 MPa) and a critical strain range between 0.4% and 0.6%. However, they display strong mechanical anisotropy, with low transverse tensile strength and limited resistance to delamination due to weak adhesion between the substrate and metallic layers.[5]

In the context of fusion magnet design, high-temperature superconductors enable new, more compact designs for fusion reactors due to two main technical advantages over LTS[6]:

- **Higher critical magnetic fields**, which is crucial since the power density in a tokamak scales with the fourth power of the magnetic field ($P \propto B^4$);
- **Operation at higher temperatures** (>4 K), which offers a wider thermal margin, helping to withstand neutron heating and reducing cryogenic system complexity and costs.

The use of HTS in nuclear applications has been considered promising, as they allow for a higher central magnetic field B_0 (approximately twice that of LTS coils). Additionally, HTS enables either more compact central solenoids (CS) for easier construction or more powerful CS coils to increase plasma duration. While several projects are already underway, many uncertainties remain, particularly regarding the effects of increased magnetic field on structural components.[7].

This behavior is further illustrated in the figure below, which shows the critical current density J_c as a function of the applied magnetic field for various state-of-the-art superconductors. It is evident that HTS maintain significantly higher J_c at high fields compared to LTS materials like Nb-Ti and Nb_3Sn.

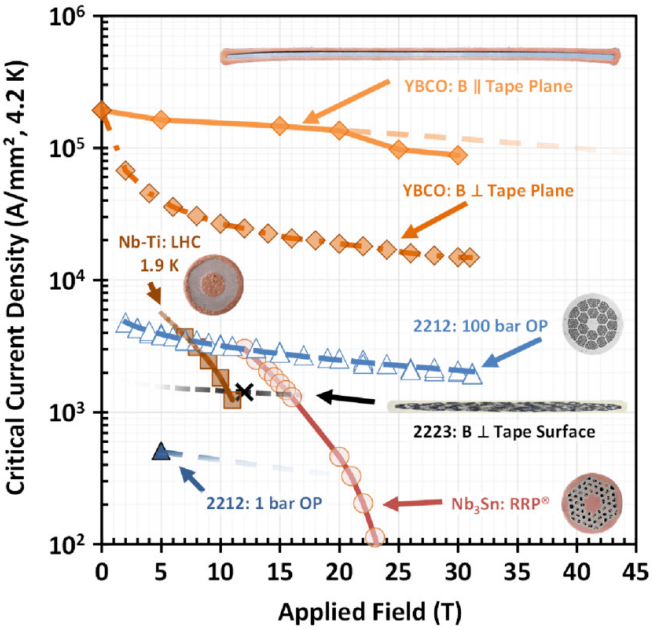

Figure 2.2: Comparison of the critical current density J_c as a function of the applied magnetic field for various superconducting materials[8].

An additional advantage of HTS materials is their relatively high critical temperatures (up to 77 K), which allows preliminary electrical tests to be performed using liquid nitrogen. This coolant is far more cost-effective, widely available, and easier to handle than liquid helium, simplifying early-stage material characterization.

While preliminary tests can be conveniently carried out at 77K using liquid nitrogen, HTS materials typically exhibit significantly enhanced performance at lower temperatures.[9]
Therefore, in demanding applications such as fusion magnets, they are often operated at cryogenic temperatures around 4–20 K, using helium-based refrigeration systems. It should be noted that the results obtained in this study, conducted using only liquid nitrogen, are not fully representative of the final operating conditions of the conductor at lower temperatures. Performance parameters such as critical current density J_c are expected to improve significantly when the material is operated in helium-cooled environments.

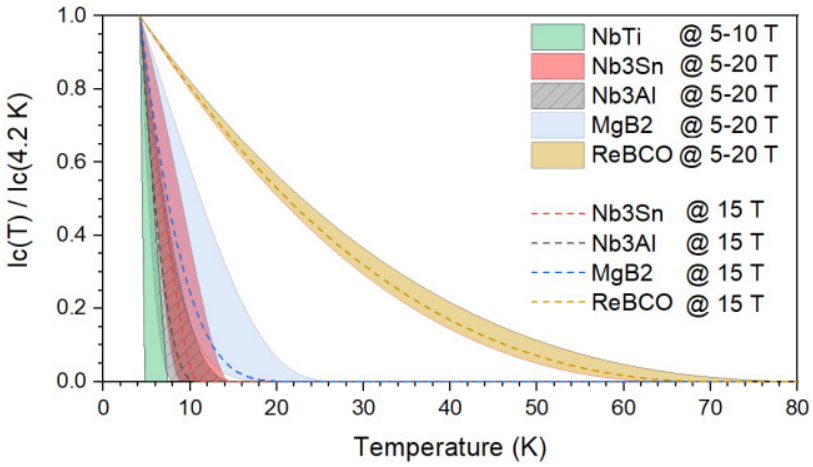

Figure 2.3: The variation of normalized critical current as function of temperature and magnetic field for REBCO (HTS) and several LTS.[9]

The results presented in this report pertain solely to the properties of the conductor tested in liquid nitrogen and in the absence of external magnetic fields. In subsequent phases of the project, the prototype will also be tested in liquid helium and under applied magnetic fields, in order to fully characterize its performance under conditions closer to those of its intended applications. These additional tests will provide a more accurate assessment of critical parameters such as the critical current density J_c and help optimize the conductor for operation in demanding environments.

Chapter 3

Conductor Assembly

3.1 REBCO: Structure and materials

HTS tapes are typically fabricated as thin films of superconducting material deposited onto a flexible substrate. The tapes are stacked and brazed together, with copper layers added to both the top and bottom of the stack. Figure 3.1 shows a schematic of the conductor architecture studied at CEA.

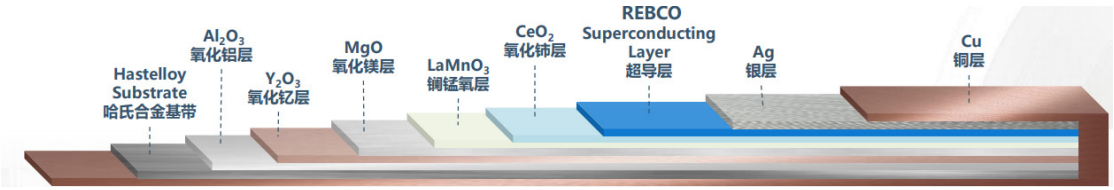

Figure 3.1: REBCO coated conductor structure (not to scale)[10].

The **REBCO** (Rare Earth Barium Copper Oxide) superconductor features a layered structure with alternating copper-oxide planes and rare-earth/barium oxide layers, resulting in strong anisotropic behavior. This anisotropy is essential for its superconducting properties, as current flows more easily along the copper-oxide planes.

Multiple layers are deposited onto a structural substrate—typically Hastelloy, stainless steel, or similar high-strength alloys using chemical or physical deposition techniques. These include textured buffer layers of metal oxides, a superconducting REBCO layer, and silver and copper stabilizing layers. Due to this multilayered, highly engineered process, REBCO tapes are commonly referred to as coated conductors.

The REBCO coated conductor is a complex, multilayered structure specifically designed to combine high superconducting performance with mechanical robustness and thermal stability. Its architecture can be described as follows:

- **Substrate:** The base of the conductor is made of Hastelloy, a high-strength corrosion-resistant alloy that provides mechanical support and flexibility to the tape.
- **Buffer layers:** A sequence of oxide layers, typically including Al_2O_3, Y_2O_3, MgO, $LaMnO_3$, and CeO_2 is deposited on top of the substrate. These layers serve several critical functions such as a chemical barrier, preventing diffusion of elements into the superconducting layer. They also improve adhesion between the metallic substrate and the superconducting layer.
- **Superconducting layer:** At the core of the tape lies the **REBCO** layer, which is responsible for the superconducting properties of the conductor. This material exhibits strong anisotropy, with superconducting currents preferentially flowing along the CuO_2 planes within its layered crystal structure.
- **Silver protection layer:** A thin silver (Ag) layer is deposited on top of the REBCO film. This layer protects the superconductor from oxidation and provides good electrical contact with the copper stabilizer.
- **Copper stabilizer:** Finally, the entire stack is encapsulated in copper, which serves as both an electrical and thermal stabilizer. The copper layer ensures current bypass in the event of a quench and increases the conductor's thermal capacity and mechanical integrity.

The tape used in the following study is produced by Shanghai Superconductor Technology, and will therefore be referred to as the SST tape.
The REBCO tape is manufactured using advanced reel-to-reel **Ion Beam Assisted Deposition (IBAD)** and **Pulsed Laser Deposition (PLD)** technologies.

In the IBAD process, an ion beam bombards the substrate while material is simultaneously deposited via sputtering or evaporation. Ion bombardment enhances adhesion and film density by modifying the surface structure and promoting compact, low-porosity film growth. The ion energy also stimulates recrystallization and reduces defects, thereby improving the film's mechanical and optical properties.[11]

The PLD technique uses a high-energy pulsed laser that strikes a solid target, vaporizing the material and forming a plasma plume. This plasma expands toward the substrate positioned opposite the target, where the condensed material forms a thin film. This method preserves the chemical composition of the target in

the deposited film and allows precise control over the film's thickness and quality.[12]

Copper is used in HTS tapes to provide both electrical and thermal stabilization. Thanks to its high electrical conductivity, copper can carry current in the event of a quench, when the superconductor loses its superconducting state. In such situations, it provides an alternate path for the current and dissipates the generated heat, preventing damage to the conductor.
Furthermore, its excellent thermal conductivity allows for uniform heat distribution along the tape, improving the overall stability and reliability of the system.

The SST tape used for conductor fabrication has a width of 12 mm and a thickness of approximately 95 μm. Although composed of multiple functional layers, including internal copper stabilizers, the tape remains mechanically fragile due to its limited total thickness.

To make the conductor suitable for practical applications, particularly in environments where strong magnetic fields induce substantial Lorentz forces, an additional external copper layer must be added.
For this reason, CEA is developing an assembly process that integrates this external reinforcement, with the goal of producing a final conductor thickness of 4 mm.
This process must ensure both enhanced mechanical strength and the preservation of the superconducting and structural properties of the original HTS tape.

The selected structure for the conductor includes three main components:

- the superconducting tape, positioned at the center;
- the outer copper layers;
- the Sn63Pb37 alloy, used as a brazing metal to join the components.

The Sn63Pb37 alloy is used as a brazing material due to its low melting point, which allows joints to be made without compromising the properties of the superconducting material. One of the main limitations in the assembly process is temperature, which must not exceed 250°C, while the alloy used melts at 183°C.
This alloy has good wettability on copper and other metals, ensuring efficient electrical and thermal contact between the components. Additionally, it is a well-established, stable, and durable alloy, with sufficient electrical conductivity to guarantee reliable performance at the joints.

The conductor has a symmetric structure: two pre-tinned SST tapes placed

face-to-face at the center, and a 2 mm copper layer on each outer side. Here, "face-to-face" indicates that the REBCO layers inside the tapes are oriented toward the center of the conductor, where they are less exposed to mechanical stresses such as bending. This thickness was chosen based on previous thermal simulations, which showed that a thinner copper layer would not ensure sufficient heat propagation in the event of a quench.

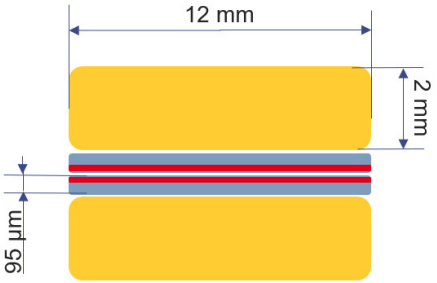

Figure 3.2: Schematic representation of the conductor: the copper plates (in yellow) make up the majority of the conductor's volume. The two SST superconducting tapes are shown in grey (not to scale), with the REBCO layer highlighted in red (face-to-face configuration).

The assembly is carried out using a heating device (figure 3.4) equipped with a clamping plate to apply pressure and promote adhesion between the components, resulting in a rigid structure. Through the application of heat and moderate pressure, the brazing metal melts and, once cooled, the final assembled sample is obtained.

Several modifications to the assembly process were implemented during the internship, with the goal of producing a more homogeneous product, with fewer defects, greater length, and reduced processing time.
For this reason, the following sections describe the different procedures adopted, highlighting their strengths and critical aspects.
The availability of multiple samples assembled using different methods also enriched the results of subsequent mechanical tests, allowing for direct comparisons between the resulting characteristics.

Summary of Obtained Samples

Across the three assembly processes, a total of 11 conductor samples were produced. These were later subjected to electrical and mechanical testing.
Each sample was identified using the code **DM**, followed by a progressive number

Assembly process	Cuivre	Length obtained	Notes	Conductors obtained
1	2 plates per side (1 mm)	50 cm	Longer process (two brazing cycles), solder material on external surface, less rigid material	DM-01
2	1 plate per side (2 mm)	1 m	Higher rigidity, less brazing material used, faster. Risk of damage during copper rolling	DM-02-03
3	1 plate per side (2 mm)	3 m	Longer conductor obtained, less risk of damaging the components. Need to pay extreme attention to alignment	DM-04 to 11

Table 3.1: Summary of the three conductor assembly processes.

3.2 First Assembly Process

Parameters used:

- sample length: 50 cm
- heating temperature: 230°C

Materials used:

- copper plates: 4 (1 mm thick, 50 cm long, 12 mm wide). Plates with 2 mm thickness were initially considered, but the available stock presented slight curvature, which prevented maintaining the required geometric precision during assembly and brazing.
- superconducting tapes: 2 (50 cm long, 12 mm wide)
- Sn63Pb37 alloy wire
- Tix-Flux flux ($ZnCl_2$)

Equipment used:

- heated press with probes and thermometer, metal plates, and silicone pads
- adhesive tape, scissors, and utility knife

The process begins by cutting four copper strips, each 50 cm in length.
Two 1 mm-thick copper strips are then paired together to create the 2 mm external layers. The Sn63Pb37 wire is coiled between them so that it will melt during the heating phase and bond the plates together. The ends of the wire are secured using adhesive tape to keep it in place. This step requires special attention to alignment, as any misalignment can lead to inhomogeneities in the final structure.
The same procedure is repeated for the second pair of 1 mm plates, and the samples are then placed in the press for heating.

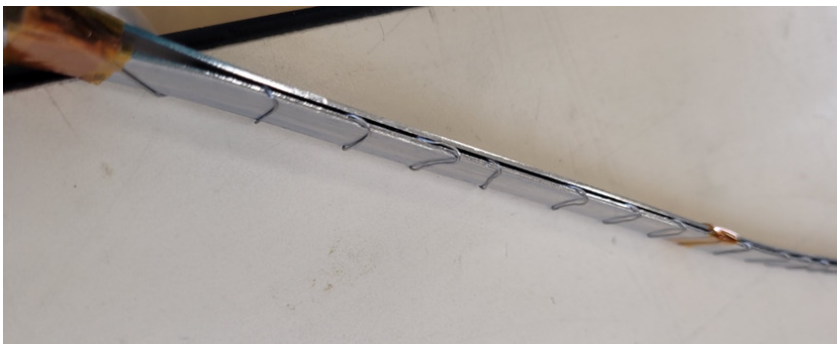

Figure 3.3: Copper plates with Sn63Pb37 wire coiled between them before the brazing process in the press.

The samples are inserted into the press, and additional metal plates are placed on top to achieve the thickness required for proper press closure. The central and lateral screws are tightened accordingly.
The heating probes and thermometer are inserted into their dedicated slots heating at the set temperature of 230°C—sufficient to melt the alloy. Once brazing is complete, the system is left to cool, either naturally or with forced ventilation, then the bolts are loosened and the plates are removed.

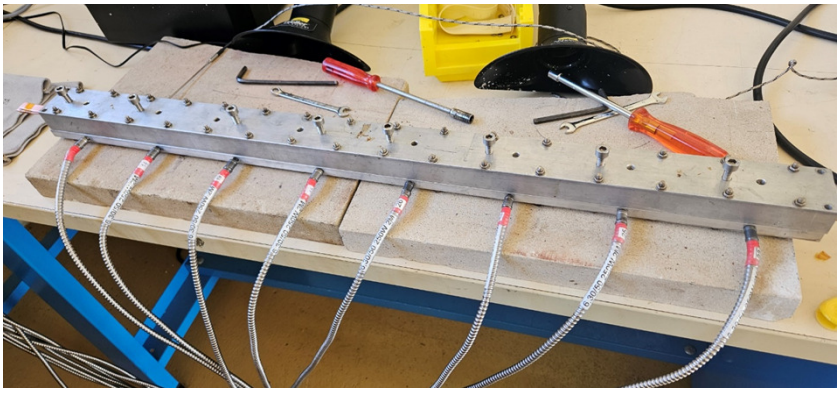

Figure 3.4: Heated press with thermal probes. Fume extractors are positioned near the press due to the toxicity risk associated with the lead content in the filler metal.

The superconducting material is inserted between the copper plates. Two superconducting SST tapes, each 50 cm in length, are cut and marked to correctly identify the side containing the superconducting layer. This step is essential to ensure a face-to-face REBCO configuration, which offers improved mechanical properties.
All components are then aligned and the brazing wire is placed between the pre-bonded copper plates and the superconducting tape
The assembled sample is inserted into the press, this time using silicone pads as protective layers, and subjected to the same thermal cycle described above.

At this stage, a significant amount of alloy overflow was observed—greater than in the previous phase—likely due to an excessive amount of filler metal used.
Finally, the sample is carefully cleaned with ethanol and prepared for testing. Some terminal sections were cut off to allow polishing and metallographic analysis, resulting in a final conductor length of 40 cm.

3.3 Second Assembly Process

The second assembly process maintains the same core philosophy as the previous one but introduces several key modifications aimed at improving sample quality and optimizing the production workflow.

Main modifications:

- Use of 2 mm thick copper plates. The presence of a rolling mill allowed these plates to be flattened prior to assembly, making them suitable despite their initial curvature;

- Use of thicker Sn63Pb37 alloy wire with a diameter of 2 mm;
- Total sample length: 1 m.

To facilitate the preparation of the copper plates, a rolling mill was used, as the plates were initially too curved and rigid to be flattened manually.

Figure 3.5: Rolling mill used to flatten 2 mm thick copper plates. The applied pressure must be low enough to correct the initial curvature without significantly altering the final plate thickness.

During the rolling process, the plates showed a tendency to shift laterally, resulting in non-uniform thickness. A guiding system is therefore recommended to limit this movement and ensure consistent output. Additionally, the rolling caused more flattening than expected, which could negatively impact the mechanical properties of the final conductor.

In addition to the copper plates, the Sn63Pb37 alloy wires (initially 2 mm in diameter) were also passed through the rolling mill, producing thin strips approximately 3.5 mm wide and about 220 μm thick.

The flux (Tix-Flux) was applied to both sides of the superconducting tapes as well as to the inner surfaces of the copper plates. The elements were then assembled in the following order:

Copper plate – two parallel Sn63Pb37 strips – superconducting tape – superconducting tape – two parallel Sn63Pb37 strips – copper plate

As shown in the following figure, all elements were held in place with adhesive tape.

Figure 3.6: End section of the conductor during alignment. The grey area on the left shows the HTS tape, ending just before the copper plate (at the bottom). The two thin Sn63Pb37 strips, obtained from the rolling mill, are also visible. All components are held in place with adhesive tape.

The assembly was then brazed using the heated press under the same operating conditions described previously, with silicone pads used to ensure mechanical protection and uniform pressure distribution.

Once the process was completed and the system cooled, the adhesive tape was removed and the sample surface was thoroughly cleaned.

Again, an excessive overflow of brazing material was observed along the edges. For future samples, it is recommended to use a single brazing strip per side with a reduced thickness and greater width, to achieve a more controlled distribution of the molten metal.
Since the Sn63Pb37 wire was not coiled in this process, no soldering residue was present on the outer surface of the conductor. Moreover, as there was no need to pre-braze the copper plates together, the inner part of the conductor also contains less filler material, as shown in the schematic below:

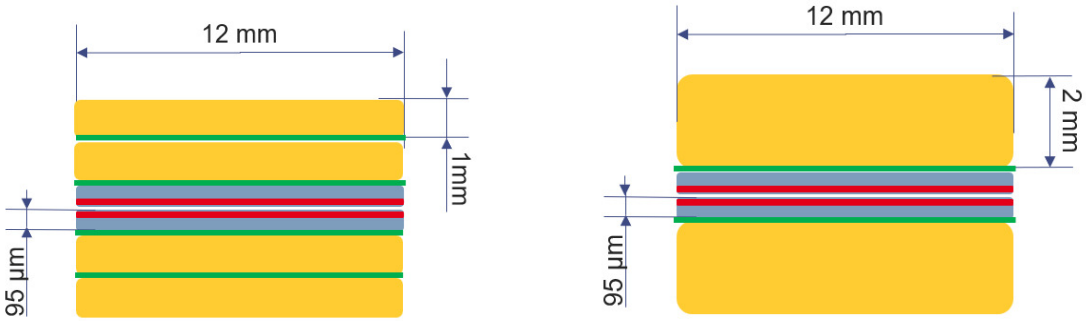

(a) Assembly method 1 **(b)** Assembly method 2

Figure 3.7: Cross-sectional schematics of the conductors. The green areas indicate the regions where the soldering alloy was inserted.

A reduced amount of brazing alloy leads to greater rigidity and improved resistance to deformation. Furthermore, this approach eliminates the need for two separate heating cycles in the press, significantly reducing the total assembly time. It also avoids the alignment issue encountered with the 1 mm copper plates in the first process, thereby improving the reproducibility of the results.

From the initial 1 m-long conductor, two 40 cm samples were obtained. This allows for all conductors to have the same test length, while preserving small sections for metallographic analysis.

3.4 Third Assembly Process

The third and final assembly process builds upon all elements introduced in the second process, with two key improvements concerning:

1. the use of the rolling mill;

2. the total conductor length achieved.

In fact, thanks to a custom guiding system, the rolling mill was used more effectively to prevent irregularities in the copper plate cross-section during processing. This also allowed for better control of the mechanical stress experienced by the material, reducing the risk of damage.

As for the length, three identical heated presses were connected in series to assemble a 3-meter-long conductor.

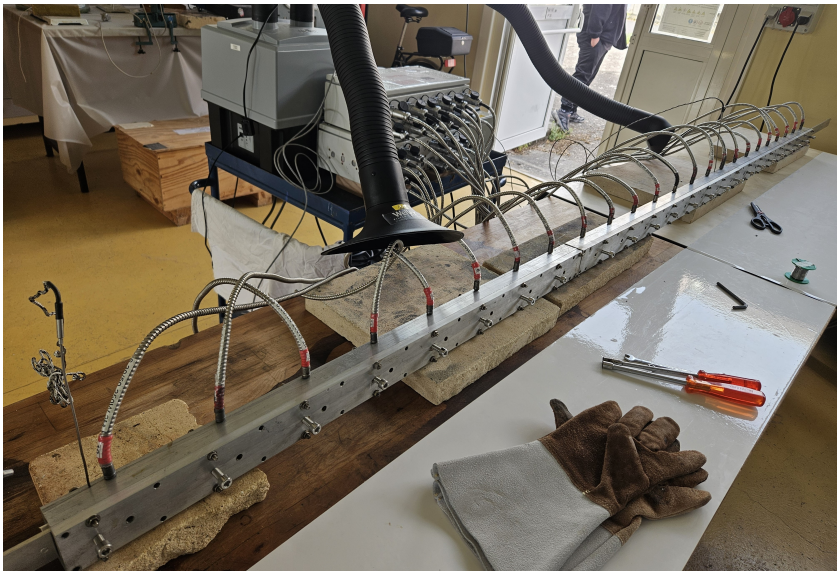

Figure 3.8: Setup used for assembling the 3-meter-long conductor, consisting of three heated presses connected in series.

The same operating parameters as in the previous processes were used, but greater care had to be taken with the alignment. As the conductor length increases, it becomes increasingly difficult to ensure that all layers remain properly aligned and that the physical and electrical properties are uniform along the entire length.

Once the process was completed, it was possible to obtain six samples from the 3-meter-long conductor for subsequent testing.

This last assembly process is the fastest, allows for greater lengths of the final conductor (important for testing the winding) and ensures good reproducibility of the process. The following chapters will highlight how the mechanical characteristics are also better than those of conductors obtained with the first two assembly processes.

Chapter 4

Metallography

A metallographic study was planned as an essential step in the characterization of the conductor. This analysis enables the examination of the geometry of each component, the evaluation of their internal structure, and the identification of any discontinuities along the interfaces.
The HTS tapes provided by the manufacturer must be examined to evaluate porosity, structural discontinuities, and edge quality. Additionally, the thickness of each layer within the composite material must be measured to verify its uniformity. Special attention must also be paid to the materials added during the assembly process, including the filler metal and the external copper laminate.

The metallographic study requires prior sample preparation, which involves polishing the surface to obtain a flat and smooth finish suitable for microscopic analysis.
Initially, the sample undergoes a precise polishing procedure to achieve a flat and smooth surface. This ensures that the microstructure is clearly visible under the optical microscope without distortion from surface roughness. Polishing is typically carried out in multiple stages, starting with coarse abrasives and gradually moving to finer ones to eliminate scratches and surface defects.

Figure 4.1: Polishing machine used to prepare samples for metallographic analysis.

Once polished, the sample is examined under an optical microscope to identify any defects introduced during the assembly process, such as cracks, voids, misalignments, or inclusions. The size, shape, and distribution of these defects are measured and documented for further analysis.

Additionally, the thickness of the brazing layer is evaluated to ensure the joint is uniform and of sufficient quality. By assessing both the structural imperfections and the brazing thickness, the metallographic analysis provides critical information on the reliability and performance of the assembled components—supporting improvements for future manufacturing processes.

Two samples obtained from the first assembled conductor were analyzed, observing both the cross-sectional area (4x12 mm) and the longitudinal section.

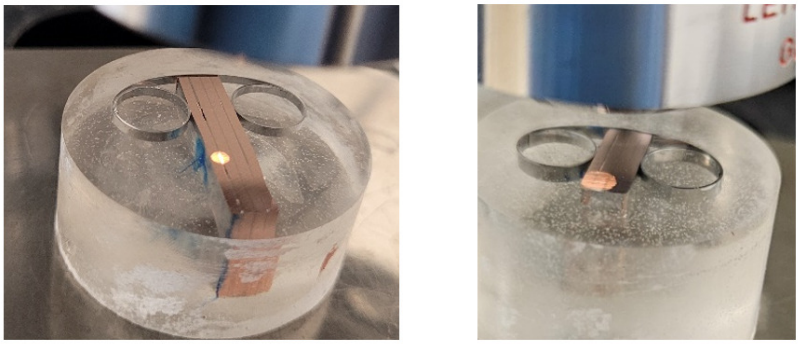

Figure 4.2: Sections of the conductor (Assembly Method 1) observed under the optical microscope. On the left: longitudinal section; on the right: cross section.

Due to technical issues with the microscope, the first images obtained were captured only with a cellphone, but they still allow the identification of the different components characterizing the conductor.
However, this approach does not provide a clear image of the geometry of the various elements and does not allow for measurements.

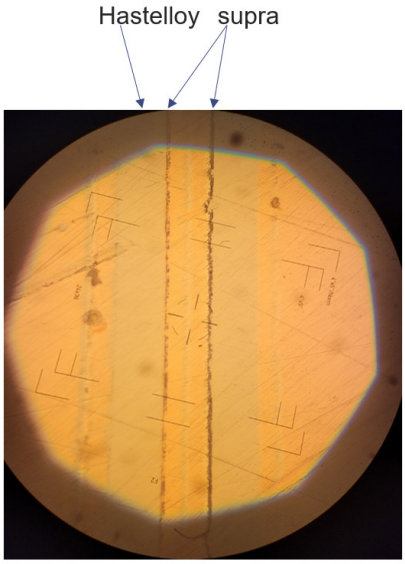

(a) Cross-sectional view. The two HTS tapes in face-to-face configuration are visible, with their internal components clearly distinguishable.

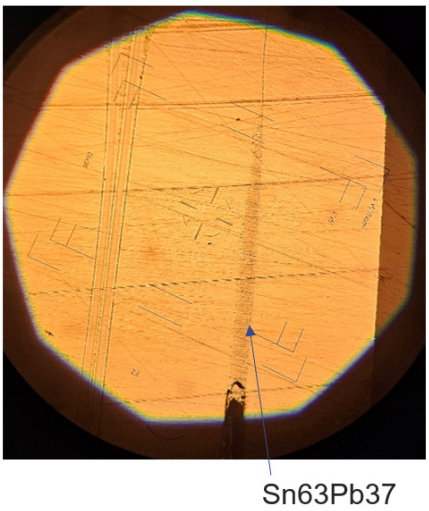

(b) Longitudinal view of the sample, showing comparative thicknesses between the solder layer and the superconductor.

Figure 4.3: Images obtained by photographing the polished samples under the optical microscope.

In image (a), the gray region corresponds to the Hastelloy substrate, while the black layer represents the REBCO, responsible for the superconducting properties. This interface is particularly critical, as it may be susceptible to damage from the flux during the brazing process.

In image (b), the result of the brazing between the two 1 mm copper sheets can be seen. The Sn63Pb37 solder layer appears quite thick—especially at the bottom—while being thinner at the top. This may be due to the use of coiled solder wire, which may not have melted and spread uniformly during heating. Additionally, the pressure applied by the press may not have been evenly distributed along the length of the conductor, contributing to non-uniform thickness.
At the bottom of the image, a void is visible, indicating a local absence of solder,

which could affect the mechanical and electrical properties of the joint.

Once the technical issues with the equipment were solved, it was possible to repeat the polishing process and obtain clearer images of the samples.
The following images all refer to cross sections of the conductor, as they are of greater interest for our analysis.

The final stage of the metallographic polishing process was carried out using a 1 μm diamond suspension. This step ensured the removal of any remaining surface scratches from previous polishing stages and produced a smooth finish on the sample surface.

Initially, the focus was placed on the analysis of the REBCO tape in order to identify its individual components and measure their thickness.

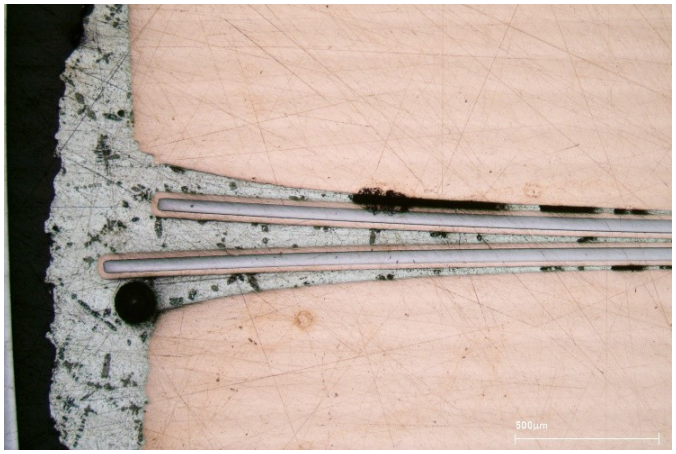

Figure 4.4: Left end of the conductor: the two copper blocks added during assembly (top and bottom) and the two REBCO tapes in the central region can be identified. Final polish using 1 μm diamond.

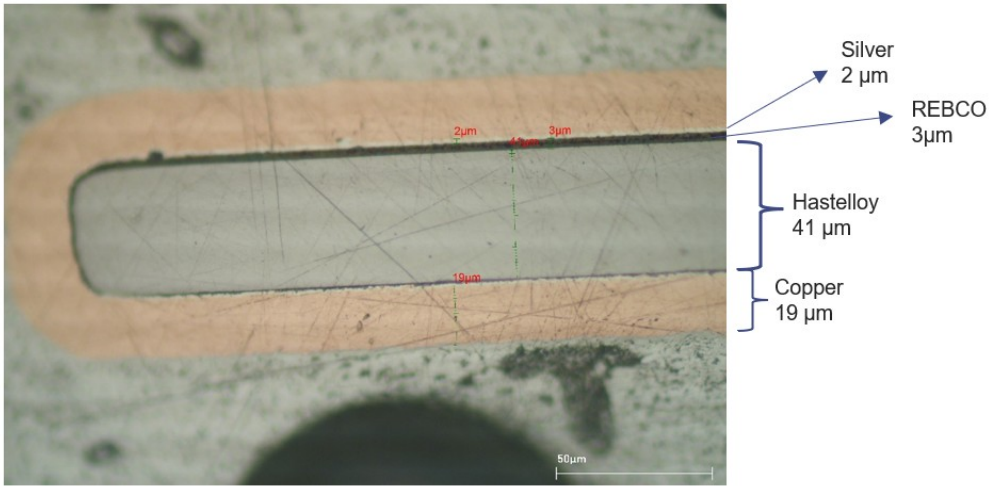

Figure 4.5: Magnification of the REBCO tape area circled in the previous image. The thicknesses of the individual elements are indicated, measured using the software.

As shown in Figure 4.4, the ends of the conductor tend to exhibit an excess of brazing material, and uniform compression is not guaranteed as in the central region. Moreover, the lower REBCO tape appears slightly misaligned with respect to the upper one, which could affect the conductor's properties.
When analyzing the individual layers, it can be observed that not all of them are easily distinguishable (Figure 4.5). In particular, the REBCO and buffer layers cannot be differentiated. The Hastelloy and copper components represent the majority of the conductor's cross section, as also indicated by the manufacturer's data.

Once the components of the REBCO tapes were identified, it was also possible to analyze the brazing added during the assembly process. In particular, both the REBCO tape–REBCO tape region and the REBCO tape–copper region need to be examined.

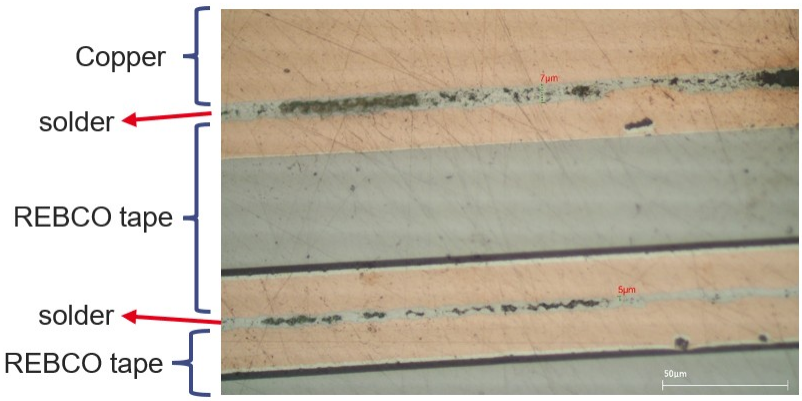

Figure 4.6: Cross section of the conductor. The various components and brazed joints can be identified. The SnPb layer between the REBCO tape and copper has a thickness of 7 μm, while between the two REBCO tapes it is 5 μm.

The image above shows an example of a region in the cross section of the conductor where good brazing was achieved. It appears fairly uniform, and the brazing material thickness is small while still ensuring good adhesion between components.

However, in other areas of the section, zones with significantly different characteristics can be observed, as shown in the figures below.

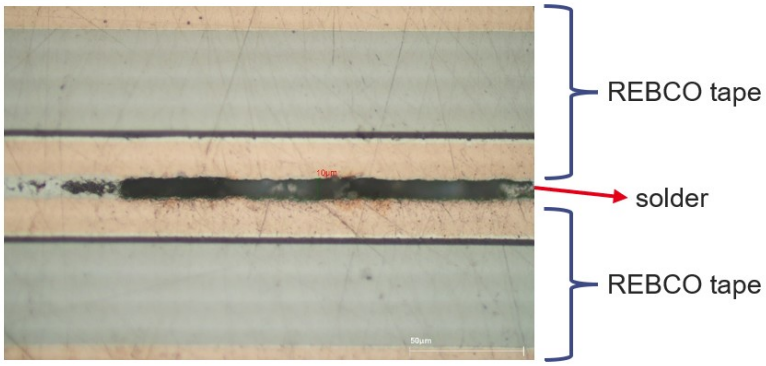

Figure 4.7: Cross section of sample DM-01. Brazed area between the two REBCO tapes showing non-uniform solder distribution. The solder layer thickness is approximately 10 μm.

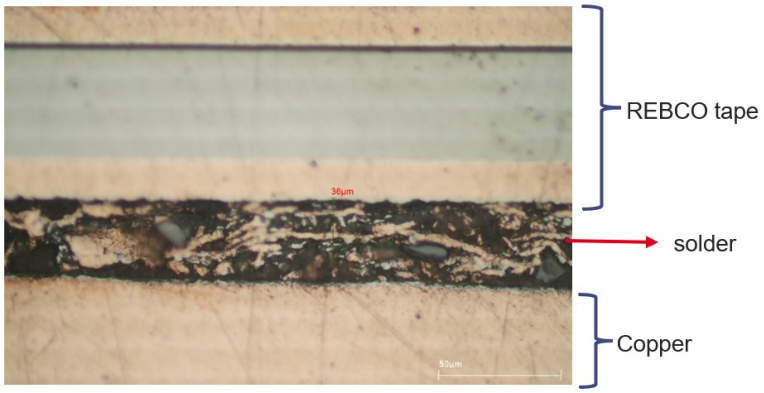

Figure 4.8: Cross section of sample DM-01. Brazed area between the REBCO tape and copper. The solder layer thickness is approximately 36 μm, with evidence of partial delamination.

In these examples (Figures 4.7 and 4.8), related to sample DM-01 obtained using the first of the three assembly processes, it can be seen that some areas exhibit a lack of brazing material or signs of delamination. These non-uniformities can affect both the mechanical and electrical properties of the conductor. In fact, incomplete adhesion between components may fail to provide the thermal and electrical stabilization necessary to protect the conductor during the transition from the superconducting to the resistive state. Moreover, delamination is more likely to occur during mechanical testing, leading to a reduction in critical current under lower stress or strain conditions.

This type of metallographic analysis, if performed on every mechanically tested sample, could help identify the reasons why conductors produced using different assembly techniques yield different results. Due to limited time availability, it was not possible to perform this analysis on the other samples, so it remains an important task for future stages of conductor characterization.

Chapter 5

Electric tests

5.1 Critical-current measurements

In order to define the critical current of the assembled superconductors, it is necessary to perform electrical tests in liquid nitrogen (77K). This type of test allows us to evaluate the critical current, defined as the maximum current that a superconductor can carry without losing its zero-resistivity property.

5.1.1 Critical current criteria

Because the voltage–current characteristic is a curve, the value of the critical current (Ic) depends on the definition. It also depends on the magnetic field, the temperature, and the strain the superconductor experiences. There are various methods to define the value of Ic:

- **The electric field criterion**: A reference electric field value (typically 1 μV/cm) is defined, and the critical current is determined as the current at which the voltage drop across the conductor reaches this threshold. This method is widely used and provides consistent, reproducible results.
- **The resistivity criterion**: This approach defines I_c based on the onset of finite resistivity. It is commonly applied in magnet engineering for comparing conductors. However, it can be problematic across a wide range of magnetic fields: at high fields, the voltage signal may fall below the instrument's noise floor; at low fields, the voltage may exceed thermal stability limits.
- **The offset criterion**: This method combines aspects of both the electric field and resistivity criteria. It defines the critical current as the point where the V–I characteristic becomes linear (ohmic). While it can offer useful insights,

it is less standardized and less commonly used in routine critical current measurements.

In our work, we adopted the electric field criterion for determining the critical current of our HTS conductor, which reaches values up to approximately 1200 A. This criterion was chosen due to its robustness, standardization, and compatibility with high-current measurements. It provides a clear and practical definition of I_c that facilitates comparisons with values reported in literature and ensures reproducibility across different experimental setups.

The voltage at which the critical current is determined does not depend on the magnitude of the current itself or on the diameter of the sample under test. Instead, a fixed critical voltage level is chosen, and the critical current is defined as the current at which the V–I curve intersects this criterion line.
The measured voltage depends on the distance between the voltage taps along the superconductor. For this reason, the criterion is typically expressed in terms of electric field (voltage per unit length) along the conductor. Ideally, the electric field value should reflect the operating conditions that the superconductor will encounter in its intended application.

Although the criterion most commonly adopted for the evaluation of the critical current is 1 μV/cm[13], there is currently no officially standardized method for determining the critical current of HTS conductors. Furthermore, a comparison of various studies on critical current measurements reveals the use of both lower (e.g., 0.1 μV/cm)[14] and higher (e.g., 10 μV/cm)[15] electric field criteria than the conventional value.

In our case, the data obtained during the experimental tests were analyzed using three different criteria: 1 μV/cm, 5 μV/cm, and 10 μV/cm. The reason behind the choice of these specific values will be discussed in the following sections.

5.1.2 Measurement Principles

For transport measurements, electrical current must be introduced directly into the sample. It is essential that the sample is securely mounted on the sample holder and that good electrical contacts are made without inducing mechanical strain. In this context, the details of sample mounting, thermal contraction, contact quality, and heat extraction become critical for reliable measurements.[16]

Most samples used for transport measurements are shaped, cut, or patterned into elongated geometries (such as wires, tapes, or strips) with uniform cross sections to ensure consistent current distribution.

The main requirements for the sample mounting system are:

1. To provide uniform and stable temperature control of the sample.
2. To eliminate mechanical stress caused by differential thermal contraction between the sample and the holder.
3. To minimize electrical noise due to induced voltages and magnetic pickup by keeping the effective voltage-tap loop area as small as possible.
4. To ensure well-designed current and voltage contacts, maintaining sufficient spacing between each current contact and the nearest voltage lead to guarantee uniform current distribution in the region between the voltage taps.
5. To provide firm mechanical support, which is particularly important during critical current measurements where large magnetic Lorentz forces can act on the sample.

A correct measurement of electrical resistance, especially under cryogenic conditions, requires the elimination of spurious voltages due to the resistance of connecting wires and contacts. In the two-contact method, both current and voltage are carried by the same leads, causing an overestimation of the measured voltage due to potential drops in the wires and contacts. To avoid this issue, a four-contact system is adopted, where two independent leads are used exclusively to measure the voltage directly on the sample, while the other two supply the current. This way, the detected voltage depends solely on the intrinsic resistance of the sample, ensuring more precise and reliable measurements, as required in low-temperature transport experiments.

When testing a sample immersed directly in a liquid cryogen, temperature measurement and uniformity along its length are generally not problematic due to the excellent heat capacity and temperature homogeneity of the bath. Under these conditions, or when only the ends of the sample need to be thermally anchored (the uniform-temperature condition is fulfilled), a sample holder with high thermal conductivity is not strictly required. Therefore, one can choose almost any material for the sample holder, provided its thermal contraction closely matches that of the sample.

Careful sample mounting, reliable electrical contacts, and uniform thermal conditions are essential when measuring the critical current. Since the critical current defines the maximum current a superconductor can carry without losing its superconducting properties, any disturbance such as temperature gradients, mechanical stress, or parasitic resistances can significantly affect the measurement. The four-contact technique isolates the sample's intrinsic voltage drop by eliminating lead and contact resistances, thereby improving accuracy. Furthermore, the sample

must be mechanically supported to withstand thermal contraction and magnetic Lorentz forces, which can otherwise induce quenching or measurement errors at high currents. Thus, meticulous preparation and control of the experimental conditions are fundamental to obtaining reliable and reproducible critical current data.

When choosing the wire diameter for the voltage taps on the sample, it is recommended to use wires significantly thinner than the sample itself. Three key length scales must be considered[16]:

- **Length 1:** This is the contact length between the current bus and the sample. It must be sufficiently large to ensure that Joule heating at the contact interface remains within acceptable limits.
- **Length 2:** This is the distance from the end of the current contact to the nearest voltage tap. It needs to be long enough to allow the current exiting the contact to fully distribute across all the inner filaments of the conductor before reaching the voltage tap. If this length is too short, the voltage taps will detect spurious voltages caused by current still crossing the resistive matrix.
- **Length 3:** The spacing between the voltage taps defines the sensitivity of the electric field measurement — the greater the separation, the larger the potential difference that can be measured.

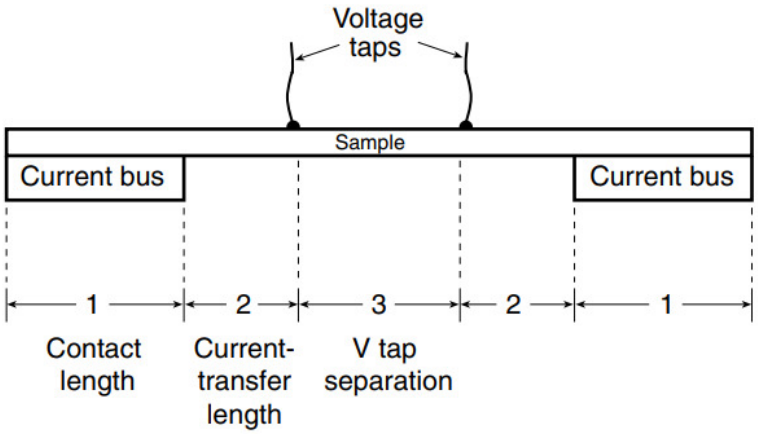

Figure 5.1: Relevant lengths for voltage-tap placement and current-contact lengths[16]

The design of the sample holder must ensure that Length 2 is sufficiently long to allow the current to cross the resistive matrix and uniformly fill the superconducting filaments. If this is not ensured, large current-transfer voltages will appear and mask the intrinsic superconducting behavior we aim to measure.

In such cases, the current-transfer voltage typically manifests as a large ohmic voltage, reflected by a linear voltage-current characteristic

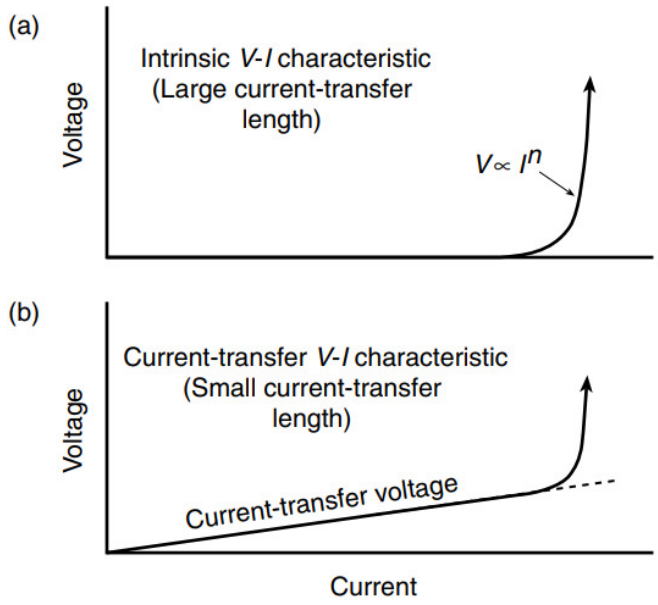

Figure 5.2: Influence of current-transfer voltage on the voltage V vs. current I characteristic of a superconductor: (a) typical intrinsic V–I characteristic measured with a long current-transfer length between the voltage taps and current contacts; (b) V–I characteristic altered by a (typically linear) current-transfer voltage measured on a sample instrumented with a short current transfer length[16]

To minimize these spurious voltages, the sample holder should be designed so that Length 2 is sufficiently long. In post treatment data paragraph we'll see how the placement of the voltage taps will lead to different graphs due to the border effects.

The voltage-current relationship becomes increasingly nonlinear as the parameter n increases. For typical high-quality conductors, n falls within the range of approximately 20 to 50, where higher values indicate sharper transitions and better performance. The current transfer length, which characterizes how far current travels through the stabilizing matrix from one filament to another, is directly influenced by multiple factors.

A high n value results in a steeper V–I curve, which causes the current to transfer over a shorter distance. For electrical contact during testing, a practical method involves using a predefined layout of contact pads on the film surface, aligned with a matching array of spring-loaded pogo pins. This design minimizes mechanical stress on the electrical leads during sample changes and ensures reliable connections.

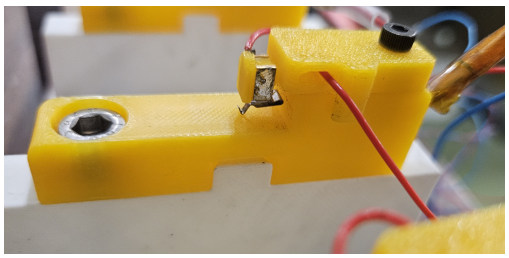

(a) Pogo pins, designed to be movable and adjustable on the conductor surface for flexible voltage tap positioning.

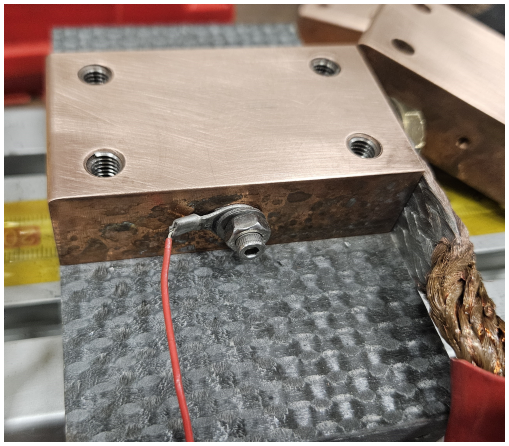

(b) Voltage taps used for the ADI, directly connected to the copper blocks supplying the current.

Figure 5.3: Voltage tap configurations used during experimental electrical testing.

In our specific setup, the pogo pins could be repositioned to vary the distance between potential leads and to select among multiple voltage tap configurations. We employed two pairs of pogo pins per sample to simultaneously acquire two voltage measurements, providing redundancy in case one pair failed. This flexibility allowed for a faster and more reproducible assembly process during testing.

Among the various techniques available for determining the critical current of a superconductor, the most practical and widely used is the transport method. This approach involves applying a current through the sample while monitoring the voltage drop along its length, enabling a direct measurement of the V–I characteristic.
Ideally, superconductors exhibit a sharp transition from a zero-resistance state to a resistive state as the current reaches the critical value, I_c.
To quantitatively describe the measured electric field as a function of applied current, the experimental data are fitted using the following empirical relation:

$$E = E_0 \cdot L \cdot \left(\frac{I}{I_c}\right)^n + R \cdot I + U_{\text{off}} \tag{5.1}$$

where:

- E is the measured electric field,
- L is the distance between the voltage taps,

- I is the applied current,
- I_c is the critical current obtained from the fit,
- n is the exponent that characterizes the non-linearity of the V–I curve,
- R accounts for any residual resistive (ohmic) contribution,
- U_{off} is a constant offset voltage representing noise or background signal.

To accurately determine the critical current and account for current-transfer voltages, it is important to trace the V–I curve as far as possible without burning the sample due to the quench transition.

The current is typically increased until a certain voltage level is reached, beyond which continuing the ramp could lead to thermal runaway. This point, which depends on both the stability of the sample and the magnitude of the applied current, marks the limit of safe operation during the measurement.
For high-current bulk samples, this reversal voltage is often limited to a few microvolts due to their lower thermal tolerance, whereas thin-film superconductors generally allow higher voltages in the millivolt range, thanks to their lower critical currents and higher surface-area-to-volume ratios that improve cooling efficiency. In practice, the quench point is often identified during the first measurement cycle, after which the reversal point is adjusted accordingly.

To prevent damage, a fast and reliable thermal-runaway protection system is essential. The risk of thermal runaway is significantly reduced when testing is performed in liquid nitrogen rather than liquid helium, since the critical heat flux for the transition from nucleate boiling to film boiling is substantially higher in liquid nitrogen. Moreover, the higher heat capacity of materials at liquid-nitrogen temperatures limits the temperature rise during transient events, making the system more robust against disturbances such as slight sample movement.[16]

Another useful tool for identifying experimental issues during data acquisition is the shape of the V–I curve itself, which can reveal several types of problems depending on its deviation from the expected behavior. In an ideal case, the curve is highly nonlinear and fully reversible, allowing for a precise and unambiguous determination of the critical current. Reversibility also confirms the absence of significant heating or mechanical strain effects during the measurement. However, deviations from this ideal shape may signal specific issues.
For instance, a rounded or more linear curve at low voltages can indicate the presence of current-transfer voltages caused by the finite resistance of the matrix material near the current contacts, especially when the voltage taps are placed too close to those contacts. Such an artifact alters the apparent V–I characteristic and

can lead to an underestimation of the critical current. In automated measurements, current reversal is often triggered when the measured voltage exceeds a set threshold, and to check for reversibility, the down-ramp is performed using the same protocol as the up-ramp. Analyzing the curve shape during both directions of the ramp provides insight into possible thermal or contact-related issues that may affect measurement accuracy.[16]

5.2 Experimental Procedure

The electrical characterization of the conductor was carried out through a series of cryogenic tests using a dedicated measurement setup immersed in liquid nitrogen (77 K). This system is designed to monitor the electrical behavior of the sample enabling us to correlate critical current performance with structural deformation of the conductor.

Before starting any measurements, the system must be correctly powered and prepared. This begins with switching on the general power supply, followed by activating the main control unit. Meanwhile, the liquid nitrogen tank is filled, and the test bench is assembled. The bench is capable of hosting up to three samples simultaneously.

The test bench is composed as follows:

- **Base support**: a 3-meter-long structure that accommodates up to three 40 cm-long samples for simultaneous testing. It is equipped with handles at both ends to allow easy insertion into the liquid nitrogen tank.

- **Copper blocks**: These serve both as mechanical clamps and as current contacts. Each block features four threaded holes used for screwing the parts together to ensure proper clamping and alignment of the conductor.

- **Connection cables**: These are attached to the outer face of the copper blocks via screws and connected on the other end to the current source. They are insulated with a plastic sheath and supply current from both ends of the conductor.

- **Pogo pins**: As described in the previous section, these voltage probes are positioned on the surface of the conductor and provide localized voltage measurements. For each tested conductor, two pairs of pogo pins are used in a configuration that allows the measurement of two voltage signals: U_1, U_2 (see schematic below). Then another pair of voltage taps is responsible for the measurement at the level of the power supply blocks (U_{ADI}).

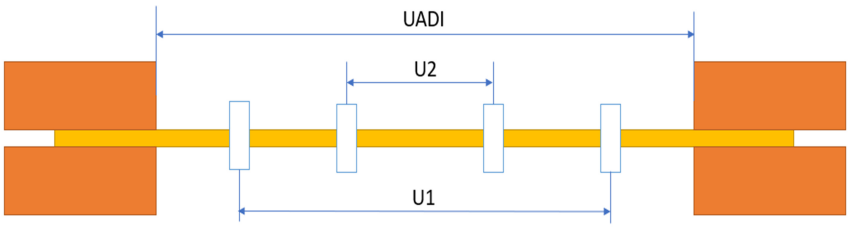

Figure 5.4: schema pogo-pins

Once the support structure is prepared, the samples are mounted following the procedure detailed below.

Each copper surface involved in the contact area is first cleaned using an abrasive cloth to remove oxide layers, then wiped with ethanol to ensure surface purity. Small indium wires are then placed between the copper blocks and the sample to enhance both thermal and electrical contact and to compensate for any surface irregularities during mechanical clamping. A thin layer of graphite lubricant is applied to prevent the indium from sticking to the copper block.

The surface of the superconductor is also cleaned to remove oxide layers before assembly. The sample is placed between the copper blocks, with additional indium wires applied on top. The blocks are then tightened to securely fix the sample in place. The pogo pins are then positioned and locked, ensuring good contact and accurate voltage acquisition. The distances between the voltage taps are measured precisely, as these values are used to compute electric field values during data analysis.

(a) DM-01 conductor before surface cleaning. Since it was assembled using method 1, the deposited SnPb layer also had to be removed.

(b) DM-01 conductor after surface cleaning with abrasive cloth.

Figure 5.5: Cleaning of the conductor prior to electrical testing. The process removes surface oxides that could compromise electrical conductivity.

Once assembled, the test bench is slowly immersed into the liquid nitrogen bath. After immersion, the copper ends of the sample are connected to the current source, and testing is performed one sample at a time.

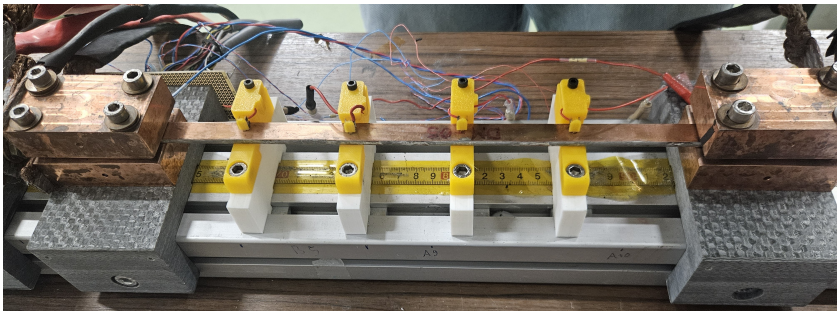

Figure 5.6: Test bench fully assembled with conductor mounted between copper blocks. The current leads and pogo pin voltage probes are connected and ready for immersion into liquid nitrogen.

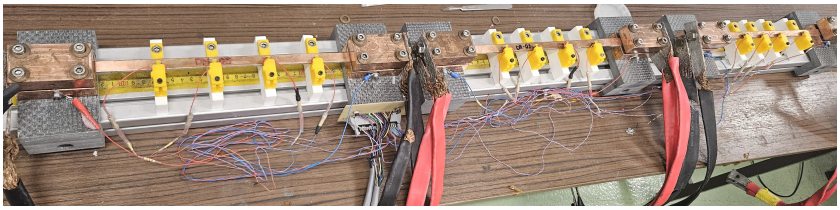

Figure 5.7: Full 3-meter test bench configured for simultaneous testing of up to three conductors. The modular design allows independent measurement and monitoring of each sample.

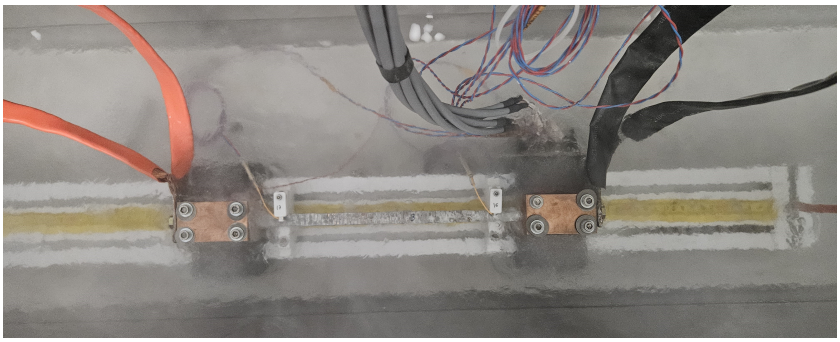

Figure 5.8: Immersion test bench into the liquid nitrogen bath

Voltage and current signals are acquired using a dedicated LabVIEW interface. The sensors are connected to a data acquisition system that communicates with the control PC. Wiring configurations for each of the three sample positions are documented in the LabVIEW Excel guide.

After connection, the LabVIEW software is launched and the operation of each pogo pin is verified. Voltage offsets are applied on each channel and the power output is enabled. Upon activation, voltage spikes should appear on the screen, confirming system responsiveness.

A preliminary current ramp up to 10 A is performed in order to verify the electrical stability of the system. During this ramp, the U_{ADI} signal is monitored.

In principle, if the superconducting layer were the only conduction path, no voltage increase would be expected during this test. However, a small linear drift is typically observed. This behavior is attributed not to the REBCO layer itself, but to resistive contributions from the copper feed blocks and the external copper layer of the conductor, which the current crosses before reaching the superconducting layer.

To quantify this effect, we estimate the resistance of the junctions by measuring the total voltage variation ΔU_{ADI} over the 10 A current ramp. This yields a typical value of the resistive drop in the copper contacts, expressed in $\mu\Omega$, which can then

be subtracted from subsequent measurements. This correction allows us to isolate the intrinsic voltage response of the conductor, and to define a corrected signal on which we can reliably base the protection threshold.

To ensure the safety of the sample and equipment, three voltage protection limits are defined:

- For U_1 and U_2: the limit is set as 50 μV/cm multiplied by the distance between voltage taps.
- For U_{ADI}: a fixed maximum of 1.5 mV is imposed.

These protections are activated prior to running any measurement.

The actual test consists of a controlled current ramp up to 1700 A, applied at a rate of 20 A/s. If any of the protection thresholds are exceeded, the ramp is automatically interrupted and the current is decreased at a controlled rate of 50 A/s. Between each ramp, the system is brought back to zero current before restarting. Typically, three complete ramps are performed for each sample.

Upon completion of all tests, data is saved, the power supply is turned off, and all electrical connections are safely disconnected. The recorded signals are then analyzed to determine the critical current of the conductor and to evaluate how mechanical assembly and sample quality influence its performance under operational conditions.

5.3 Data Analysis

The data obtained from the previously described tests contain information on:

- time (s);
- current (A);
- voltage (V) from all potential taps.

Therefore, it is necessary to use a program capable of processing the data. During the internship, Python was used, as an initial script was already available. However, it required adaptation since the data acquisition system had been modified (making the resulting file format incompatible), and the script was not suited for critical current measurements involving such high values, as in the case of our conductor. The script first identifies and separates the available data, and uses an additional file containing the distance values of the potential taps (U1, U2, UADI).
It then proceeds to plot the current versus time graph and identifies the different current ramps, which are subsequently analyzed individually.

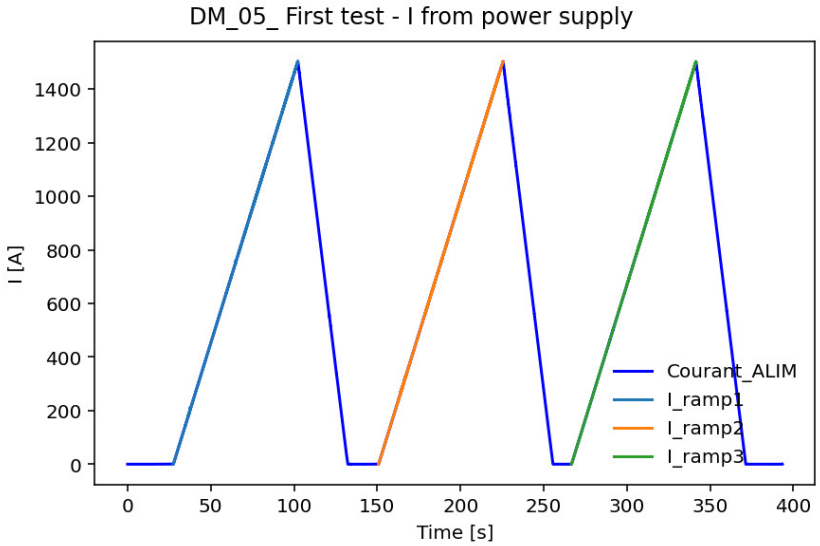

Figure 5.9: Example current ramp: I vs time

The script then filters the data of each individual ramp, extracts the values corresponding to voltage (U), current (I), critical voltage (U0), and the distance between the pogo-pins (L), and applies the formula (5.1) to perform a fit. The fitting yields the following parameters: critical current (Ic), exponent (n), residual resistance (R), and offset voltage (Uoff).

This procedure is repeated for each ramp and for each potential tap. The corresponding curve resulting from the fitting equation is then plotted over the dataset in an E-I graph. This type of plot is preferred because the criterion used to define the critical current is expressed in microvolts/cm, making it independent of the distance between the voltage taps (thus allowing comparison of the values obtained from the different pogo-pins during the test).

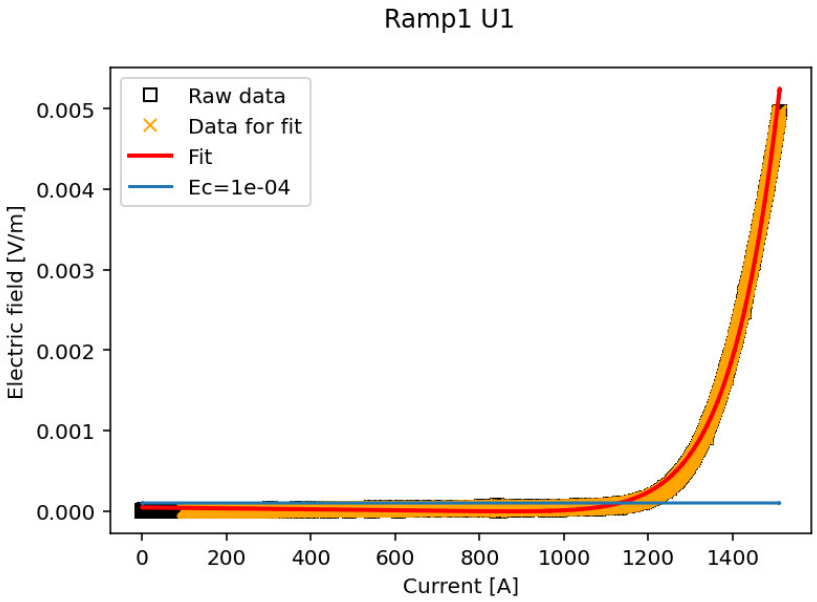

Figure 5.10: Example fitting result

As shown in the figure above, the yellow points indicate all the data considered for the fitting, the red curve represents the fitting result, and the light blue line corresponds to the threshold value (E0) used to determine the critical current.

The results obtained for each potential tap (U1, U2, UADI) are saved, and an average is computed across the various ramps (including the corresponding standard deviation).

During the data processing of the different tests, numerous errors occurred that initially prevented the completion of the fitting procedure, causing the script to fail. However, over the course of the internship, the script was progressively improved, making the process more robust and capable of handling the different cases and variability of the acquired data.

5.3.1 Fitting correction

By analyzing the results obtained from the post-processing, several considerations were made and, during the internship, modifications were applied to the program to take into account certain elements that prevented a rigorous analysis of the obtained values.

All the considerations and plots discussed in this section refer to the analysis of the same electrical test (i.e., the dataset remains unchanged), which we will refer to, for simplicity, as the "study test". The study test corresponds to the critical current measurement performed on the DM-01 sample after it was subjected to a

tensile load of 100 MPa prior to the electrical test.

This test was chosen because:

- data acquisition from all three voltage taps was successful;
- no degradation was observed after the mechanical test;
- the first current ramp had low background noise and interference;
- the second current ramp showed higher interference (used to study standard deviation and measurement accuracy);
- the test was among the first performed (these considerations began to develop in the early months of the internship and evolved over time).

Dataset limitation

By examining the generated plots, it became clear that even though the code was capable of performing a fit, the resulting curve was not always representative of the original data—particularly near the threshold defined for the determination of I_c.

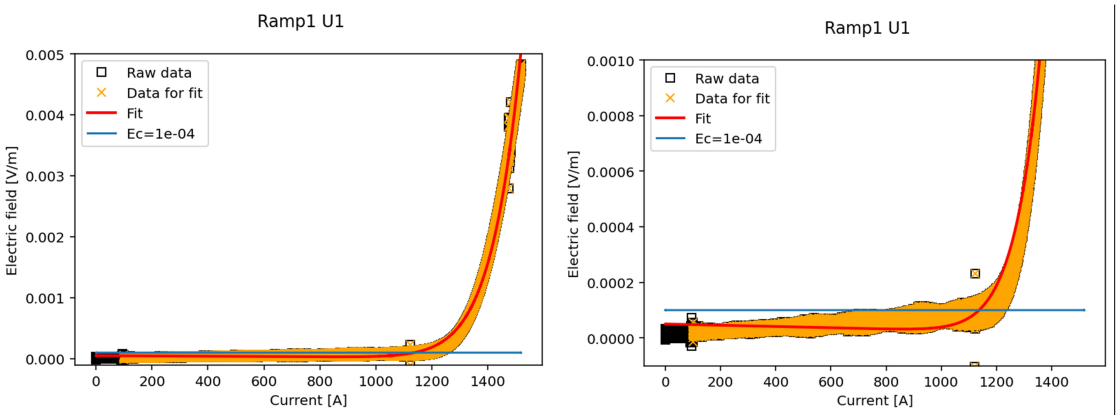

(a) Complete view **(b)** Close up

Figure 5.11: Study test – first fitting results

The images above refer to the same graph; in figure (a), no apparent issues are visible in the resulting plot. However, zooming in on the region close to the threshold defined by the criterion $E_0 = 1\,\mu\text{V/cm}$ reveals that the fitted curve does not pass exactly through the average values of the test data. This leftward shift results in lower critical current values than what is likely the true result. For this reason, the data processing procedure was revised, starting with a restriction of

the dataset used for the fitting calculation.

The initial results were based on the full set of data acquired during the test, which was itself limited by protection thresholds arbitrarily set at $50\,\mu$V/cm. This value allows a wide transition range without the risk of triggering a conductor quench, which is optimal; however, such a broad dataset might not be well-suited to the application of equation (5.1), which represents a model valid only near the transition's critical current.

Therefore, a filter was introduced prior to the fitting process to restrict the dataset based on voltage, limiting it to values up to 10 times the threshold criterion E_0—in this case, reducing the upper bound from $50\,\mu$V/cm to $10\,\mu$V/cm.

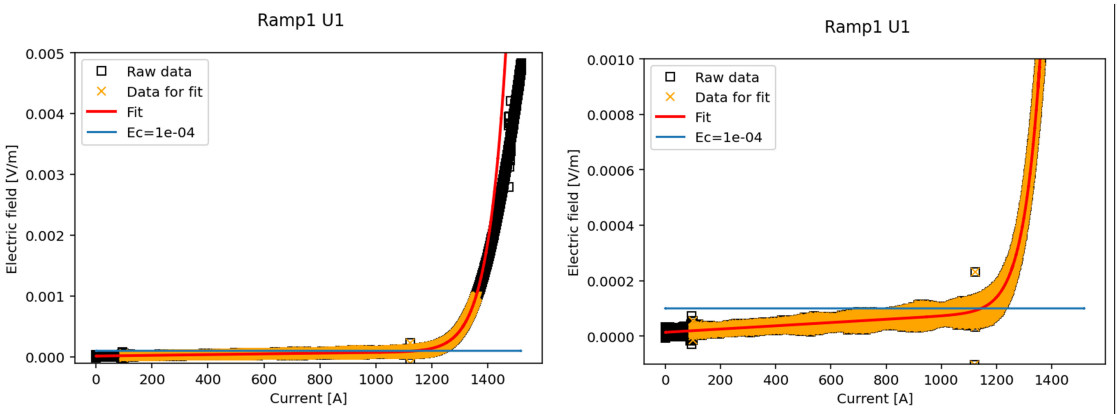

(a) Complete view **(b)** Close up

Figure 5.12: Study test - dataset filtering

Ec (μV/cm)	Fit stop	Ic (A)	n
1	no limit	1158.1	14.5
1	10 μV/cm	1230.9	22.5

Table 5.1: Comparison of fitting results with and without voltage stop criterion.

The results shown above were obtained by applying this method to the same dataset used for figure 5.11.
In black, the entire dataset is displayed, while in yellow, only the data used for the fitting process are shown.
The first noticeable difference in Figure (a) is the slope of the red line in the final part of the plot. The increased slope and thus the increase in the exponent

n—indicates that, in the filtered data, the superconductor transition occurs more rapidly, followed by a deceleration. This phenomenon confirms that the applied formula does not perfectly describe the behavior of the conductor but is instead suitable for analyzing only a limited region, after which a different model should be considered for the final part.

The second difference is shown in Figure (b): this time, the fitted curve more accurately represents the average voltage behavior in the conductor, and as a result, the critical current value obtained is closer to the actual physical value.

The results demonstrate that when using a complete dataset up to $50\,\mu$V/cm, the effects of the final slope of the transition curve dominate the behavior near the critical current criterion. Therefore, restricting the dataset proves to be a valid solution to mitigate this issue.

Critical current criteria analysis

Another observation made while analyzing the plots concerns the data dispersion in different regions of the graph.
In particular, in plot 5.12 (Figure b), it is evident that the dispersion is significantly higher in the region preceding the steep increase of the curve compared to the final segment. Specifically, the E_c line intersects the data starting from a current of approximately 800 A and extends beyond 1200 A—representing a very wide range. The situation differs in the region where voltage values exceed $4\,\mu$V/cm, where the curve has already reached a consistent slope and the voltage values are much more closely clustered.

For this reason, it was decided to calculate the critical current using different E_0 criterion values. As discussed in the previous section, it is possible to vary the value of E_0 from the commonly used $1\,\mu$V/cm. In our case, we also performed calculations using E_0 values of $5\,\mu$V/cm and $10\,\mu$V/cm.

Changing the E_0 value also implies a change in the data filtering criterion described above, since a dataset including values up to $10 \times E_0$ would again encompass the entire acquired data range, leading to the same incompatibility and offset previously discussed. Therefore, it is necessary to reduce the dataset to a range considered acceptable for achieving a good fit. In our case, this translates to:

- $10\,\mu$V/cm for the $5\,\mu$V/cm criterion (i.e., the same dataset used for the initial $1\,\mu$V/cm fitting);

- $20\,\mu$V/cm for the $10\,\mu$V/cm criterion (expanded to include data points beyond the critical voltage value).

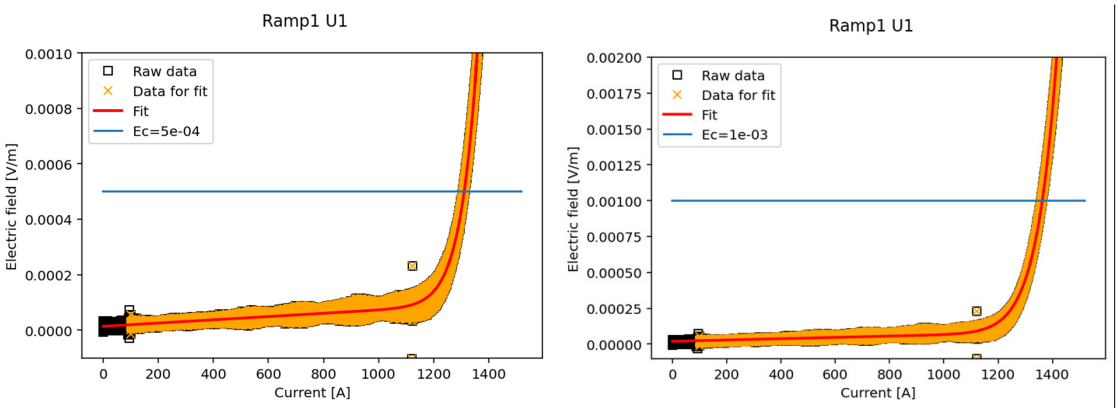

(a) Criterion 5microV/cm **(b)** Criterion 10microV/cm

Figure 5.13: Study test - application of other criteria

It is clear from these last two images that the E_c line intersects the plot over a narrow range of values. This implies that the resulting critical current value is characterized by a smaller error and is less affected by variability. On the other hand, choosing to modify the critical field criterion cannot be done without considering several important factors. First and foremost, in order to compare the results with those from other studies, it is essential to use the same criterion. Since the most commonly adopted criterion is $1\,\mu$V/cm, it will therefore be necessary to continue using it in data analysis. Indeed, it becomes evident that changing the criterion leads to a significant increase in the calculated critical current.

Nonetheless, it remains useful to retain the results obtained using the other two criteria. For this reason, the data analysis script was modified to automatically compute the critical current using all three criteria and to store the results separately.

Ec (μV/cm)	Fit stop	Ic (A)	n
1	10 μV/cm	1230.9	22.5
5	10 μV/cm	1322.1	22.5
10	20 μV/cm	1368.0	19.2

Table 5.2: Effect of different E_c and fit stop values on critical current and n-value.

Initial resistive behaviour

Upon analyzing the resistance values obtained, it became clear that they were not consistent. In the initial results (prior to dataset filtering), the resistance values

extracted from the fit using equation (5.1) were almost always negative (in the order of nano-ohms). An initial explanation could be that the resistances were so low that these values were merely the result of noise in the acquired data.

However, after filtering the dataset as previously described, the resistance values also changed—becoming positive in some cases (although still very low).

This raised the question of whether this method of resistance estimation was appropriate, as it heavily depends on the selected dataset and is not as directly observable as in the case of the critical current value. Indeed, the formula used is designed to describe the transition phase of the conductor, but it is not the most suitable method for analyzing the initial linear resistive region. For this reason, it was decided to apply a linear fit to estimate the values of R and U_{off} in the region preceding the critical current, using the following equation:

$$U(I) = R \cdot I + U_{\text{off}} \tag{5.2}$$

To ensure that this new fitting is applied only in the linear behavior region, the following process was implemented as shown in the diagram below:

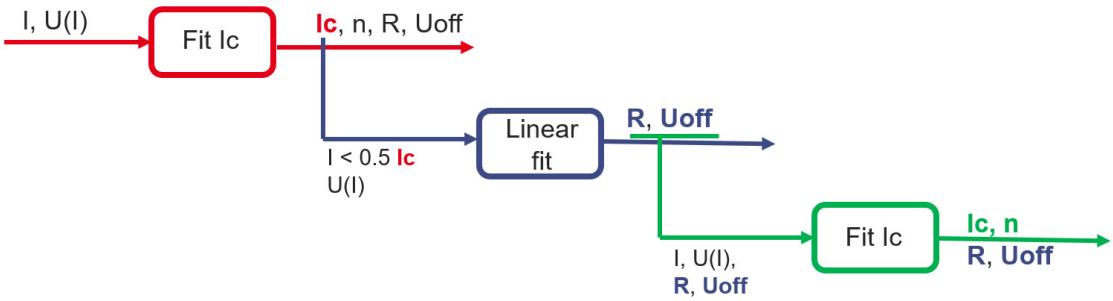

Figure 5.14: Fit process scheme

The "Fit Ic" block represents the fitting process using equation (5.1), which is rewritten below for clarity:

$$E = E_0 \cdot L \cdot \left(\frac{I}{I_c}\right)^n + R \cdot I + U_{\text{off}}$$

Whereas the "Linear fit" block refers to equation (5.2).
Following the scheme, the code first performs a fitting procedure in the same way as described in previous cases. However, this initial fitting is only used to determine the approximate range in which I_c lies. The dataset is then filtered to include only current values up to half of I_c. With this new subset—representing the purely linear resistive region—a second fitting is performed using (5.2) to obtain the resistance

and offset voltage values.

These obtained values are saved, the dataset is restored to its original state, and a third and final fit is carried out. This time, the input data for evaluating the critical current will include not only current (I) and voltage (U), but also the previously determined resistance (R) and offset voltage (U_{off}).

Since these two parameters are now inserted manually, they are treated as constants during the final fitting process and will therefore remain unchanged at the end.

	Ic (A)	**n**	**R (nΩ)**	**Uoff (μV)**
fit1	1158.9	14.5	-4.2	9.2
fit2			11.1	2.3
fit3	1173.6	15.2	11.1	2.3

Table 5.3: Fitting steps results

The table above shows an example of the results obtained at the end of each fitting block. Only the values from the third fitting (fit3) are recorded in the final results. It can be observed that by fixing the values of R and U_{off}, the values of I_c and n change during the fitting process. This procedure is repeated for each current ramp and for each voltage tap.

The table below, on the other hand, shows the resistance values calculated for the voltage taps U1 and U2, and how these values vary across the following three cases:

1. using the entire available dataset;
2. using the filtered dataset;
3. using the filtered dataset along with the pre-calculated resistance.

Ec (μV/cm)	**RU1** (nΩ) full dataset	**RU1** (nΩ) limited dataset	**RU1** (nΩ) linear fit	**RU2** (nΩ) full dataset	**RU2** (nΩ) limited dataset	**RU2** (nΩ) linear fit
1	-4.49	10.46	11.20	-6.69	0.02	0.54
5	-4.49	10.46	11.25	-6.69	0.02	0.53
10	-4.49	7.49	11.27	-6.69	-1.07	0.53

Table 5.4: Comparison of RU1 and RU2 resistance values.

The values determined using the linear fit are not affected by the dataset reduction applied during the I_c calculation, since they are extracted directly from the initial portion of the current ramp. These values can also be used to refine the definition of the critical electric field threshold.

Initially, the threshold E_c was represented as a horizontal line at constant electric field. However, this representation did not take into account the low-current resistive contribution, modeled as $R \cdot I + U_{\text{off}}$, expressed in Volts.

Considering that the vertical axis of the plot is in volts per meter (V/m), it was necessary to normalize the resistive potential with respect to the sample length L. Consequently, the threshold E_c was redefined as:

$$E_c(I) = E_0 + \frac{R \cdot I + U_{\text{off}}}{L} \tag{5.3}$$

This new formulation accounts for both the intrinsic threshold E_0 (in V/m) and the ohmic contribution, also correctly expressed in V/m.

This adjustment helps to better understand the impact of the ohmic term, and whether this contribution is significantly affected by the distance between the voltage taps and the current injection points at the ends of the conductor.

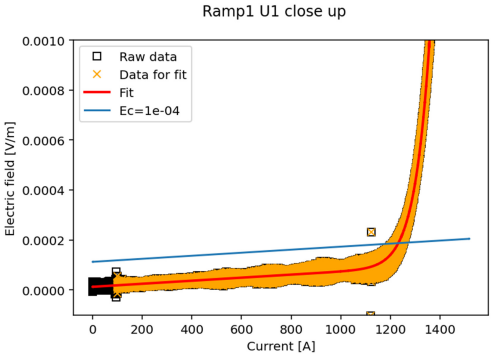

(a) Voltage tap U1 – located closer to the edges of the conductor (approximately 17 cm from the copper blocks)

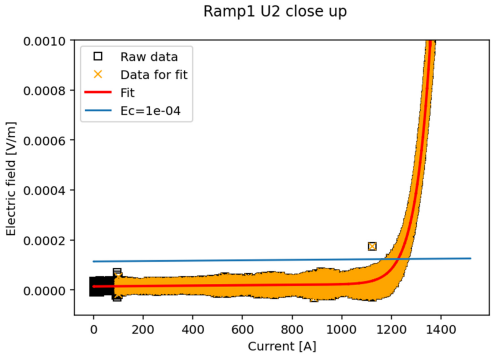

(b) Voltage tap U2 – located at the center of the conductor (approximately 22 cm from the copper blocks)

Figure 5.15: Test study – Effect of conductor resistance on the critical current criterion

From the images above, it can be observed that the effect of resistance near the edges of the conductor (a) is significantly greater compared to the central positioning. This result confirms the phenomenon previously discussed and shown

in Figure 5.2, concerning the necessary distance for current transfer within the conductor.

5.3.2 Evaluation of Measurement Precision

Considerations were also made regarding the data dispersion obtained during the tests, and criteria were sought to quantify the measurement uncertainty.
The chosen approach for an initial analysis involves considering the intersection point between the E_c line and the fitted curve, then taking a neighborhood corresponding to 10% of the voltage value.
Once this zone is isolated, the data are divided into intervals based on the delta of the current value relative to the current determined by the fitting. These deltas are then grouped into bins (the number of which can be varied depending on the desired precision), and the groups are plotted according to the density of their data population.
The critical current value I_c determined by the fit is also plotted as a dashed line, and a Gaussian function is created by fitting the population density data.
The variable μ indicates the offset between the center of the Gaussian and the I_c value obtained from the fit, while σ represents the standard deviation derived from the Gaussian fit.

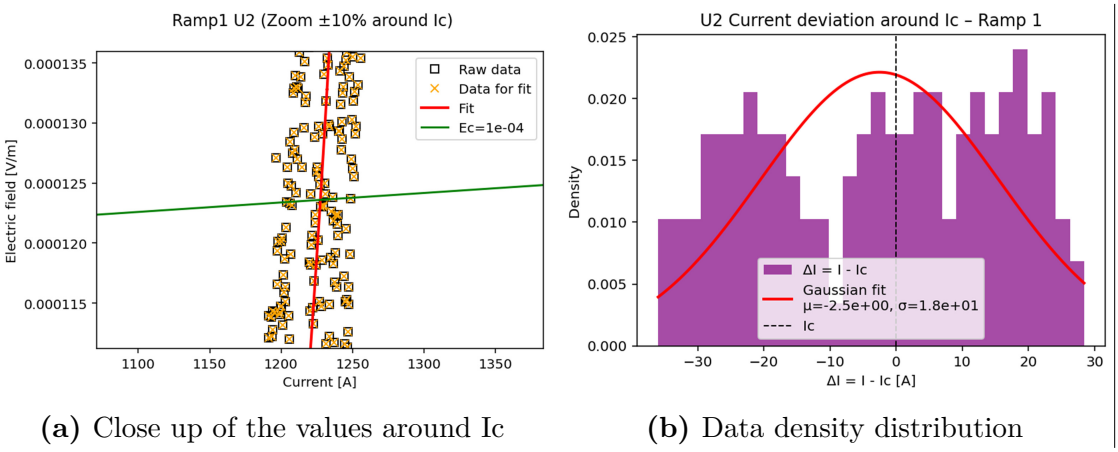

(a) Close up of the values around Ic **(b)** Data density distribution

Figure 5.16: Study test - Gaussian fit on zoomed data

As can be observed from the graphs above, the measurement precision within the 1μV/cm range results in relatively high standard deviation values. On the other hand, the value obtained does not significantly deviate from the critical current value determined by the fitting, which confirms that the previously described corrections to the fitting process have led to a reliable evaluation of the phenomenon in the transition region. The current range in this treated zone is quite broad,

exceeding 50 A.

However, this method does not always perform well in cases where measurement interference is very high. Indeed, the second current ramp of the same test was analyzed, yielding the following results:

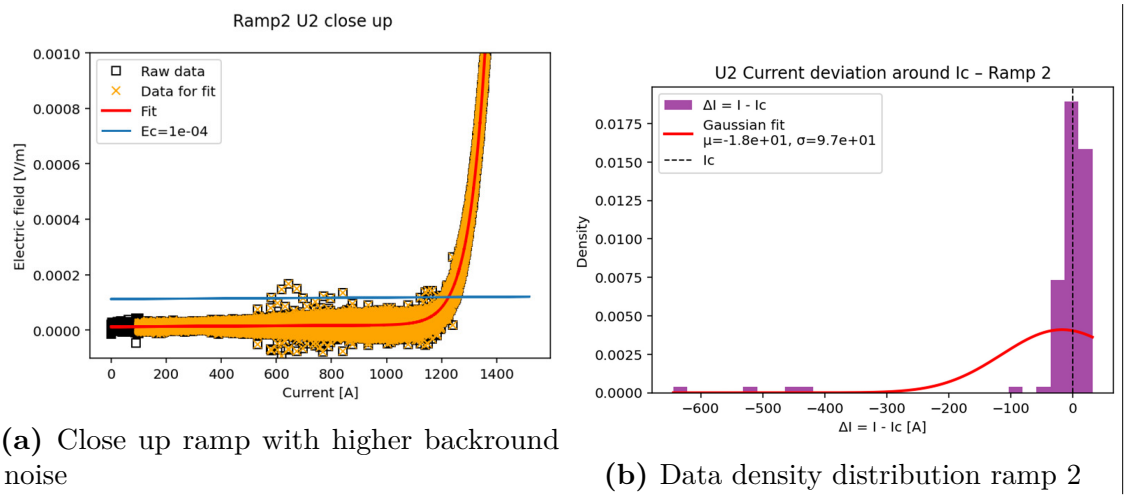

(a) Close up ramp with higher backround noise

(b) Data density distribution ramp 2

Figure 5.17: Study test - Second ramp analysis

The presence of background noise causes a signal exceeding the critical criterion E_c starting from current values around 600 A, as shown in Figure (a). This signal thus distorts the Gaussian distribution and prevents an accurate estimation of the error.
Possible solutions to mitigate this problem include:

- improving the quality of the power supply signal (although this is an expensive solution);
- filtering the acquired data, which can be done either before the fitting or only during the determination of the standard deviation;
- increasing the value of the E_c criterion, so that the noise signal does not fall within the critical current detection range.

Having already explored the last of these options, it was attempted in the analysis of the same ramp, and indeed the result is noticeably different, as shown in the image below.

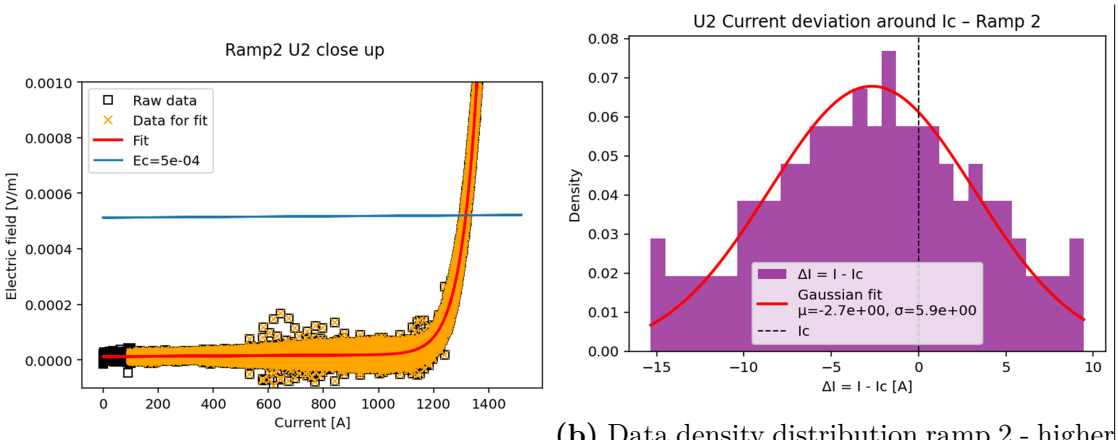

(a) Ramp 2 - higher Ec value

(b) Data density distribution ramp 2 - higher Ec value

Figure 5.18: Study test - Second ramp analysis with higher Ec value

The line representing the critical criterion this time lies well beyond the interference region, and the data distribution on the Gaussian appears more uniform. Moreover, the spread of values is within a range of approximately 30 A, confirming the higher measurement precision compared to the previous case.

Based on these considerations, discussions were held with the rest of the PEPR project team, who agreed on the method of improving the fit by precalculating the initial resistance and limiting the dataset. Some doubts were raised regarding the choice to change the criterion for evaluating the critical current, since to provide results comparable with other studies and maintain rigor, it is necessary to remain consistent with the commonly used reference system.
Therefore, the analysis of the error obtained during the tests remains an important aspect but will not be further elaborated in this report, as the focus was chosen to be on other tests and elements that represent the main core of the internship.

5.4 Current Redistribution

Another aspect analyzed was the current redistribution within the conductor. Typically, the conductor is powered from both ends (via the upper and lower copper blocks). However, during the conductor winding phase, it is required to power it from only one side, so it was necessary to characterize this phenomenon and verify if there were any differences regarding the measured critical current value.

Previous studies conducted at CEA investigated the current distribution between two HTS tapes soldered only at their ends, leaving the central section unsoldered.

In that setup, the tapes were supported by ferrite cores, and Hall probes were used to monitor the magnetic field along their length in order to infer the current sharing. When current was injected from only one end, the distribution between the tapes was found to be unbalanced, leading to a reduced effective critical current compared to the case where both ends were powered.

To assess whether the same behavior occurs in a different configuration, I carried out similar tests on my conductor, which also consists of two HTS tapes. However, in this case, the tapes are continuously soldered along their entire length and are clamped between two external copper plates. These copper layers not only provide thermal and electrical stabilization but are also expected to improve current sharing between the tapes. The goal was to verify whether this more integrated structure mitigates the current imbalance observed in the earlier setup under asymmetric current injection.

It was chosen to power only from the bottom side (configuration which in the previous study provided the worst current sharing result). It was sufficient to connect the power cables only to the lower copper block and use kapton tape on the upper surface of the conductor. The test was then carried out in a manner analogous to the previous ones, and the results are shown in the table below:

Table 5.5: Critical current and n-value results (Ec=1μV/cm) for different power input configurations

Sample	**Power input side**	I_c **(A)**	**n**
DM-10	both sides	1225.00	23.00
DM-10	bottom sides	1222.25	22.90
DM-11	both sides	1240.15	23.15
DM-11	bottom sides	1237.25	23.05

As can be seen, no significant differences were observed in the results obtained by testing the same samples in the two configurations. This allows us to consider the soldering quality sufficiently good for current sharing, and the copper support of the conductor also helps improve the current transfer between the two tapes. It should also be noted that the test was conducted on a 40 cm sample, which is considerably shorter than the lengths planned for the subsequent prototype. Therefore, such an encouraging result is expected to lead to an optimal current distribution on larger scales.

The DM-11 sample also exhibited a soldering defect: since the terminal part of the 3 m conductor—assembled using process 3—was positioned outside the heating press, one end of the conductor remained unsoldered. Despite this, the critical current measurements did not show lower values compared to the other samples

from the same conductor.

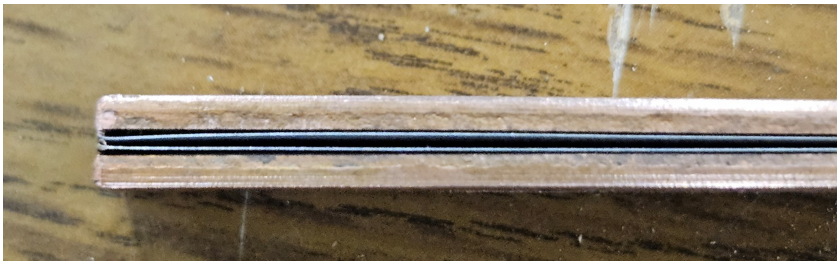

Figure 5.19: Conductor DM-11 terminal part

5.5 Consistency of Critical Current Measurements

The available data on the critical current obtained during all the tests allows for a brief analysis of the repeatability and consistency of the results across samples taken from the same conductor. This retrospective evaluation aims to explore whether different assembly methods have an influence on the dispersion of the measurements, thus providing insight into the reproducibility and reliability of the electrical characterization.

Table 5.6 reports the average I_c and n-values, along with their corresponding standard deviations (STD), for each group of samples. The samples were grouped based on their assembly method and they are part of the same initial conductor cut into pieces to obtain our samples.

Samples	**Assembly Method**	**Mean I_c (A)**	**STD I_c (A)**	**Mean n**	**STD n**
DM-01	1	1234.7	–	26.4	–
DM-02–03	2	1199.6	45.68	19.825	4.28
DM-04/09	3	1227.74	9.39	22.92	0.30
DM-10–11	3	1232.58	10.71	23.08	0.11

Table 5.6: Summary of critical current and n-value for different samples and assembly methods

The samples DM-02-03, assembled using Method 2, shows the lowest average I_c (1199.6 A) and the highest standard deviation (45.68 A), indicating a significant variability among the tested pieces. The n-value is also the lowest (19.825), with a relatively high deviation (4.28), which further supports the interpretation of poor uniformity.

In contrast, sample groups DM-04/09 and DM-10-11, both assembled with Method 3, demonstrate significantly improved consistency. Their I_c standard

deviations are below 11 A, and their n-value deviations are particularly low (0.30 and 0.11 respectively), indicating a stable and repeatable current transfer behavior. Additionally, their mean I_c values remain high, further confirming the robustness of the assembly.

Chapter 6

Tensile test

In order to perform the mechanical characterization of the conductor, a series of tests were conducted to identify the critical stress and strain thresholds beyond which the conductor's electrical performance begins to degrade.
The procedure begins with an initial measurement of the critical current under zero mechanical stress, followed by a step-by-step comparison of the critical current (Ic) measured after each mechanical loading phase.
This iterative approach, alternating between electrical and mechanical testing, enables the development of a comprehensive understanding of the conductor's mechanical behavior and allows us to estimate the limits it can tolerate.
Variations in the conductor's assembly processes were also considered, and an analysis was carried out to evaluate how the fabrication method may affect the test results.

The tensile test is one of the most commonly used mechanical tests for evaluating the strength of materials. It involves applying a gradually increasing uniaxial tensile force to a specimen until failure occurs. This test allows for the determination of key mechanical properties such as yield strength, ultimate tensile strength, and elongation at break.
In the case of superconducting conductors, the tensile test is particularly relevant, as it reveals how axial strain affects electrical performance, especially the critical current.

In this study, tensile tests were conducted under controlled conditions. After each loading cycle, the critical current was measured and compared to the reference value obtained prior to the application of mechanical stress. This methodology allowed for the identification of the strain threshold beyond which irreversible degradation of the conductor's electrical properties occurs.

Tensile tests were carried out on various samples:

- DM-01, assembled using procedure 1;

- DM-02/03, assembled using procedure 2;

- DM-05/06/07/08/09, assembled using procedure 3.

Before testing these samples, it was necessary to assess the mechanical strength of the individual components comprising the conductor.
For this reason, data on the copper used and the SST superconductor were analyzed. Regarding the latter, tensile test data already available in the literature were considered, specifically those performed on the individual superconducting tapes.
The objective of this study is therefore to verify whether the superconducting tape maintains its behavior once embedded within the copper layers of the assembled conductor.

Regarding the copper, it was decided to test individual sheets identical to those used during the assembly phase. Although it would be possible to rely on literature to determine the mechanical properties of copper, numerous variations exist due to differences in thickness, manufacturer, and the processing history of the material prior to use in the conductor (such as the rolling process described in Chapter 3). For these reasons, the first tensile tests were performed exclusively on copper sheets. This not only provided valuable data on the individual components but also allowed familiarization with the testing equipment before proceeding to tests on the actual conductors, and facilitated the development of a data analysis script for the acquired results.

To determine the tensile properties, incremental load-unload cycles were performed. From these tests, the Young's modulus was extracted (by analyzing the initial portion of the unloading curve), along with the yield stress corresponding to a permanent strain of 0.2%. The results obtained were: Young's modulus = 112.5 GPa, and yield stress = 221.99 MPa.

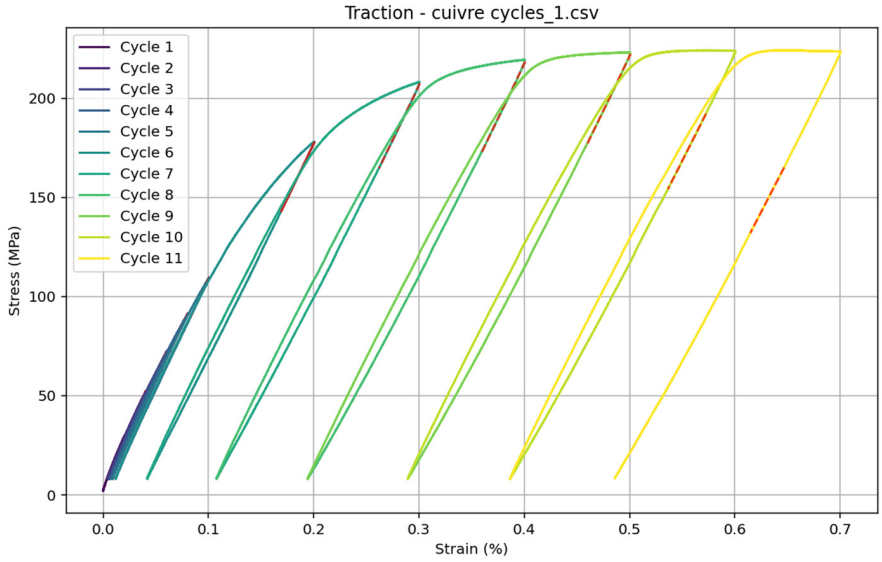

Figure 6.1: Tensile test cycles with increasing strain on a 2 mm-thick copper sheet

Subsequently, the assembled conductors were tested. Some samples (DM-01/02/03/05/07) underwent progressive strain loading cycles, while others (DM-06/08) were subjected to repeated cycles with a constant maximum strain.

6.1 Literature on the tensile properties of REBCO SST

The mechanical properties of REBCO HTS tapes have been extensively studied in the literature, with data also provided by major manufacturers and research centers. These characterizations typically focus on single superconducting tapes and include key parameters such as elastic modulus, tensile strength, and bending resistance.

However, once the conductor has been assembled—as described in the previous sections—it becomes essential to verify that the assembly process has not introduced defects or alterations that could compromise its performance. In particular, it is important to ensure that there is no degradation of mechanical properties or conditions that could promote local damage during operation. For this reason, mechanical characterization of the final assembled conductor is fundamental to ensure both structural and functional reliability.

Nevertheless, the literature provides a useful starting point to identify the approximate limit values for the material, helping to design the tests close to the critical regions and to compare the behavior of the single tape with that of the fully assembled conductor.

HTS tapes have already been examined by research centers such as the University of Twente[17], which tested the properties of several REBCO samples from different manufacturers to analyze the change in electrical performance as a function of mechanical strain. The tensile tests were carried out in liquid nitrogen to evaluate variations in properties during both loading and unloading phases.

The results obtained for two samples are shown below:

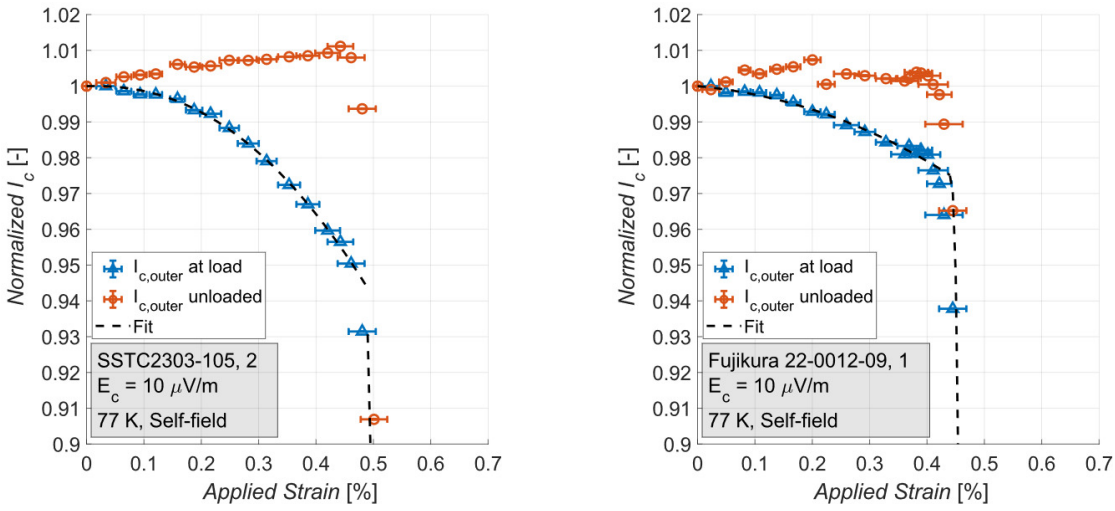

(a) Test on SST tape **(b)** Test on Fujikura tape

Figure 6.2: Normalized critical current variation as a function of strain during tensile tests[17]

As shown in the graphs, there is a clear difference between the values obtained during the loading phase (blue) and after unloading (orange). This helps to distinguish between reversible and irreversible loss of superconducting properties.
Furthermore, the degradation behavior differs between tapes from different manufacturers: in the SST case, the reduction in critical current follows a more parabolic trend, while in the Fujikura case, the transition is sharper.
In both cases, a reversible loss of critical current (typically defined as a 10% reduction compared to the zero-strain condition) occurs at around 0.45% strain. Specifically, for the SST tape—used in our tested conductors—the corresponding

value is 0.43%.
Additionally, the stress values associated with this critical strain are 709 MPa for case (a) and 626 MPa for case (b).
These values are significantly higher than the yield strength of the copper used for conductor assembly (approximately 260 MPa). This means that during testing the copper undergoes plastic deformation, and because it is soldered to the tape, it transfers this deformation to the superconducting layer.

A similar study[18] was conducted on four SST tapes soldered in a face-to-face configuration, identical to that of our tested conductor. The solder used in that case was also Sn63Pb37, and a thermal treatment was applied using a press to ensure proper bonding.
These stacked-REBCO samples were subjected to tensile tests similar to those described above, with results presented in the following graph:

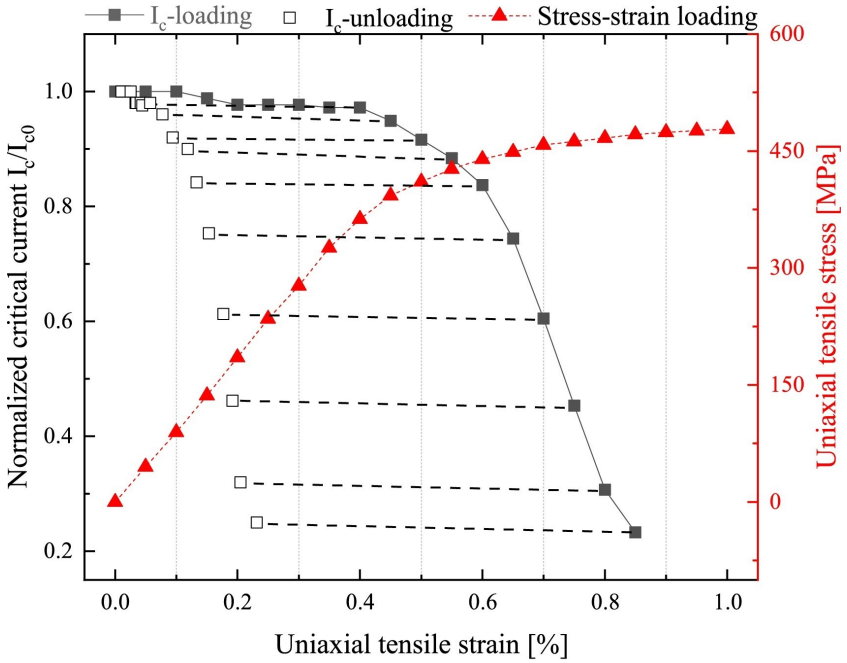

Figure 6.3: Uniaxial tensile test results of REBCO-stacked cable in face-to-face configuration[18]

The graph shows both the stress-strain curve indicating a maximum stress value of approximately 450 MPa—and the normalized critical current as a function of strain.
Unlike the previous study, which only considered conditions leading to a reversible Ic loss below 10%, this work also explores the degradation of superconducting

properties up to their near-complete loss.
Interestingly, despite the high elastic recovery observed (as seen from the distance between black and white squares), there appears to be no recovery of superconducting properties once degraded.
For instance, considering the Ic-loading point at 0.6% strain, a 40% loss in critical current is observed; the corresponding unloading point exhibits the same loss even though the residual strain is only about 0.2%.
By comparison, at 0.2% strain during loading, no significant degradation occurs, suggesting that REBCO degradation is governed not by the current strain at the time of measurement, but rather by the maximum strain experienced during the test.

Based on these findings, it is expected that our assembled conductor, composed mainly of copper. will deform under lower stress levels. However, it remains to be verified whether the Ic/Ic_0-strain curve follows a similar trend or whether degradation is influenced by the addition of copper on the sides and the fabrication process.
Specifically, we aim to determine whether a 0.5% strain leads to a 10% loss of Ic (the reversibility threshold) and whether superconducting properties are retained, even partially, up to 0.8% strain.

To analyze the data from our tensile tests, the same graphical scheme presented above was used. This visualization method allows us to display, in a single plot, the maximum stress reached, the maximum and residual strain, and the corresponding critical current loss for each tensile test.

The ideal setup for characterizing the conductors would involve performing tensile tests in a liquid nitrogen bath while simultaneously measuring the variation in electrical properties in real time. However, several limitations prevent us from conducting such tests in our laboratory:

- the testing machine is not suitable for this type of experiment, and there is no tank of appropriate size to contain liquid nitrogen;

- the electrical power supply is located too far from the testing machine.

For these reasons, it was decided to adopt a discontinuous approach by alternating tensile tests and electrical tests in a cyclic manner. This setup significantly increases the time required to complete each test, due to the need to reconfigure the critical current (Ic) test bench each time, allow the sample to return to room temperature after testing, and then prepare it again for the next mechanical test.
As critical current cannot be measured during the loading phase, all critical current values discussed here refer exclusively to the unloaded state.

6.2 Test procedure

The first step in the tensile testing process involves setting up the equipment. The upper and lower blocks of the testing machine must be screwed into place and properly aligned to allow for correct mounting of the grips.
The grips are then inserted and secured using locking pins (*goupilles*) placed in the dedicated slots.
Once assembled, the machine can be powered on, and the test parameters can be configured via the control software.
The software used is "Instron", which allows the creation of customized methods for tensile or compression testing by adjusting several parameters.
The first data to be input relates to the specimen geometry:

- total length (aligned with the tensile axis): 40 cm;
- gauge length (between grips): 30 cm;
- width: 12 mm;
- thickness: 4 mm.

Width and thickness may vary slightly between samples due to differences in SnPb distribution across the conductor or due to the copper flattening process. However, these geometric parameters are corrected during post-processing, as the analysis is based on the measured force (in kN) rather than the nominal stress provided by the software.

The control panel allows the user to set key testing parameters, such as speed (in mm/min) and the maximum limit to be reached (either in force or strain). The unloading phase can also be configured under similar conditions, or a repeated load/unload cycle can be programmed by specifying the number of cycles.

For the standard tensile tests, the loading phase was defined based on the target final strain, with the speed set to 1 mm/min for both loading and unloading. The unloading limit was typically set to 0.2 kN.

For cyclic tensile tests, different parameters were chosen: the speed was increased to 4.8 mm/min, and the unloading force limit was set to 20 MPa.

To prepare the specimen for testing, it is sufficient to measure the sections to be gripped (ensuring that the central portion corresponds to the gauge length) and properly secure the sample.
The extensometer is then positioned at the center of the sample and fixed with O-loops, ensuring they are tight enough to maintain correct positioning.

The test can then be launched and will automatically stop once the predefined values are reached. The resulting data file contains:

- time (s);
- displacement (mm) of the machine crosshead;
- force (kN);
- strain (%).

(a) Full front view of the tensile press

(b) Side view with extensometer

Figure 6.4: Tensile test setup

6.3 Data analysis

The data obtained from the tensile tests were analyzed using a Python script developed during the internship.
The first step involves plotting stress-strain curves. The strain values are taken

directly from the extensometer readings, while stress is calculated from the recorded force divided by the actual cross-sectional area measured using a digital caliper.

The script then calculates the slope of the unloading curve by using the first data points following the stress peak, allowing for the determination of Young's modulus.
If the test results in sufficient plastic deformation, a second line is drawn parallel to the unloading curve but passing through the origin and 0.2% strain. The intersection of this line with the loading curve provides the yield stress (MPa).

Additionally, if the unloading curve is incomplete, the script extrapolates it to determine the final residual strain (at 0 MPa), which is then used in the analysis of subsequent loading cycles.

A second script was developed to process data from cyclic tensile tests. It identifies loading and unloading phases by detecting local maxima and minima and calculates Young's modulus for each cycle. As before, the residual strain at the end of each test is also recorded.

Another script analyzes the CSV files from all conducted tests to generate a graph showing how the strain evolves over time, highlighting the actual strain values recorded.

Finally, a dedicated script plots stress and normalized critical current (Ic/Ic_0) as a function of both maximum and residual strain. This enables a direct comparison between mechanical and electrical test results.
The tool also allows for the comparison of different samples to determine whether variations arise from different assembly methods and to assess the repeatability of results among samples produced using the same method.

6.4 Results Obtained

6.4.1 DM-01

This section presents the results obtained for conductor DM-01, assembled using Assembly Method 1 as described in the previous chapter.
As this was the first conductor tested, the testing procedure had to be gradually adapted based on the results obtained. Initially, the goal was to evaluate the potential variation of electrical properties with respect to the stress applied during the tensile tests.
For this reason, tests were performed at 50, 100, and 125 MPa to assess the effect

of stress. Since no degradation was observed after cryogenic testing, it was decided to switch to a deformation-based approach.
The mechanical limit of the conductor was being approached, and increasing the load further would likely result in failure. The plot below shows the tensile cycles performed on the sample. It is evident that above approximately 160 MPa, the stress-strain curves exhibit significant plastic deformation.

However, since the superconducting layer is a brittle ceramic material, damage primarily occurs when the strain exceeds a critical threshold. The stress associated with a given strain depends on the geometry and materials of both the conductor and the tape; as a result, stress values cannot be directly compared across conductors with different designs. Therefore, mechanical degradation should be evaluated in terms of strain rather than stress.

The final test did not exhibit a true unloading curve because the force limit of the testing machine was reached during the test.

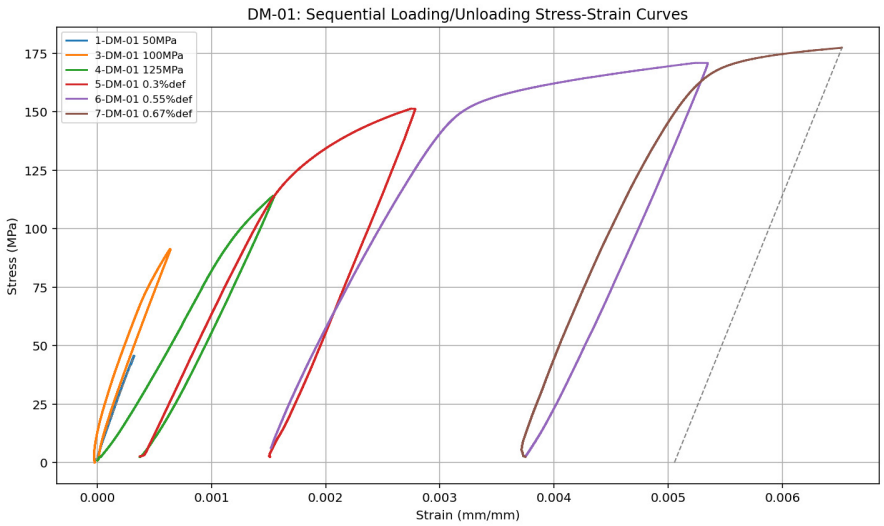

Figure 6.5: Tensile cycles - Stress-strain curve for DM-01

The results of cryogenic electrical tests conducted after each tensile cycle are shown in the following plot. The red curve represents the stress-strain relationship, marking the maximum strain reached during each test. The blue points represent the normalized critical current values (relative to the initial value before mechanical testing) as a function of the same maximum strain.
The black triangles indicate the residual strain at the end of each unloading cycle, which is relevant since electrical tests were not performed while the sample was under load (as discussed earlier, due to limitations in implementing in-situ electrical

measurements during mechanical tests).

This means the degradation values obtained refer exclusively to irreversible property loss. However, it is possible that some temporary losses occur at peak strain, which are fully recovered upon unloading.
The resulting trend clearly shows that superconducting property degradation is a nonlinear phenomenon. There is an initial plateau followed by a critical strain threshold beyond which the critical current rapidly decreases.

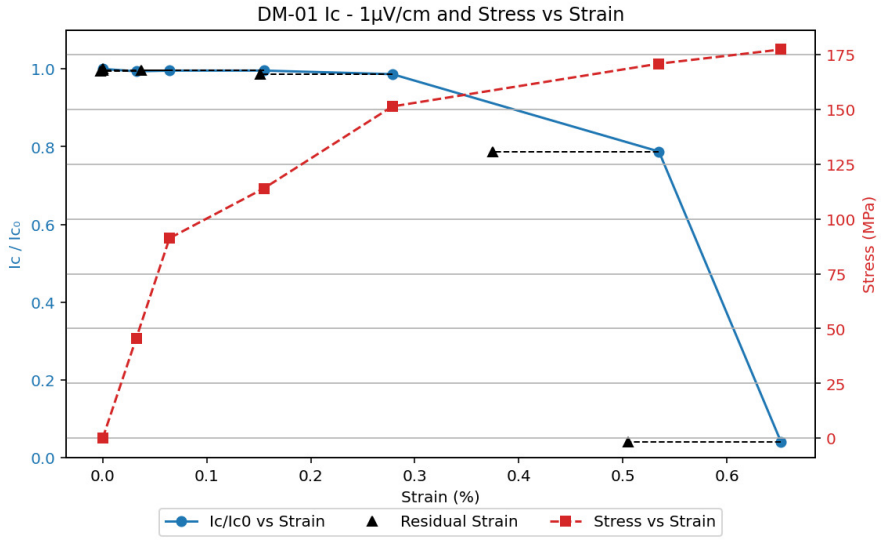

Figure 6.6: Normalized critical current vs. strain for DM-01

The results are consistent with the literature on tensile tests performed on isolated REBCO tapes, suggesting that Assembly Method 1 does not introduce degradation into the superconducting tape.

6.4.2 DM-02/03

Samples DM-02 and DM-03 were manufactured using Assembly Method 2. Tensile tests were performed on both to allow mechanical and electrical characterization. Since they were cut from the same initial 1-meter conductor, identical test protocols were applied to evaluate possible variation along the sample's length.

DM-03 was tested first, following the same procedure as DM-01, as the tests were conducted in parallel. For this reason, the stress-strain curves are initially based on stress levels, and later on strain values.
In this case, even after reaching the limit of the original load cell (at 200 MPa), the sample showed no significant degradation (again, the unloading curve was

extrapolated numerically).
A new load cell with a higher maximum capacity was used in subsequent tests.

DM-02 was tested afterward, and the loading was performed directly near the maximum strain limit that still preserved superconducting properties, based on previously obtained results.
The plots below show the mechanical and electrical test results for DM-03, followed by a comparison with the results for DM-02.

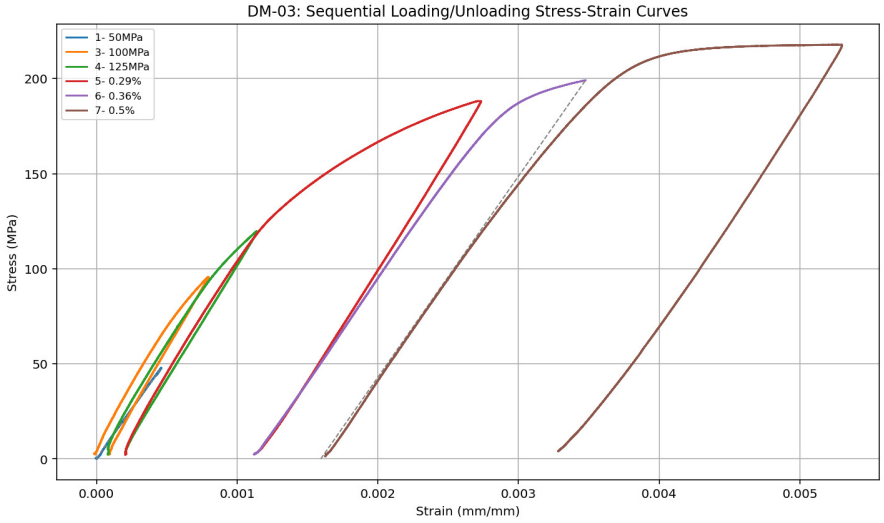

Figure 6.7: Tensile cycles - Stress-strain curve for DM-03

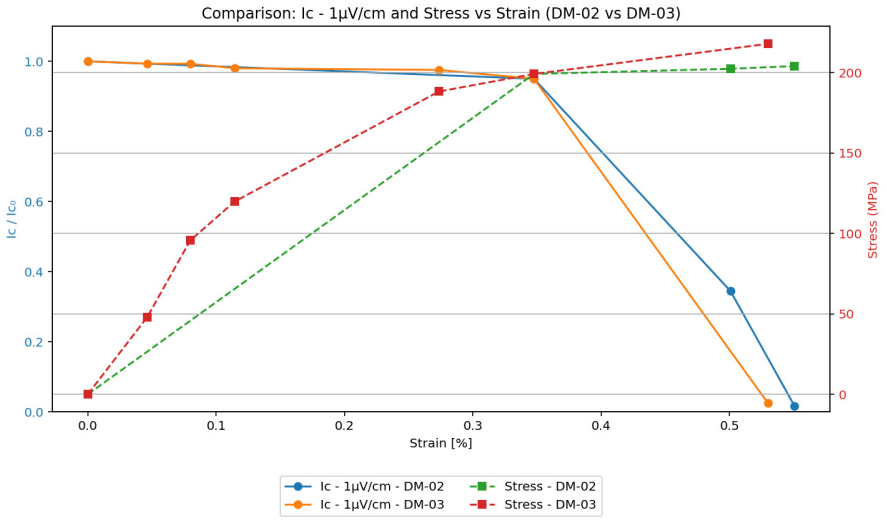

Figure 6.8: Comparison of normalized critical current vs. strain: DM-02 vs DM-03

As shown, both samples exhibit very similar results: they retain nearly all of their superconducting properties up to 0.35% strain, with total degradation occurring around 0.55%.
Mechanically, they show comparable characteristics, with yield stress values around 200 MPa, beyond which strain increases even at constant stress.

Comparison between DM-01 and DM-03

The first two samples tested did not exhibit identical behavior, either mechanically or electrically.
From the tensile tests, DM-01 showed a lower yield stress, entering plastic deformation at lower force values. This is likely due to the 1 mm copper plates having a lower yeld strength than the 2 mm plates used in DM-03. Additionally, the presence of SnPb solder layers between tapes in DM-01 may have reduced the overall mechanical strength — an effect less significant in the 2 mm copper layers. On the other hand, DM-01 retained its superconducting properties up to higher strain values than DM-03, possibly due to differences in damage accumulation during the assembly process.

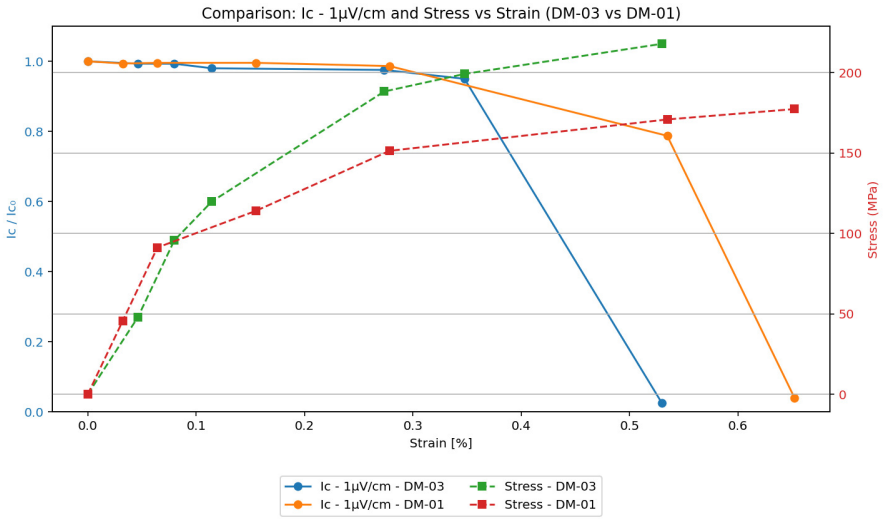

Figure 6.9: Mechanical and electrical comparison between DM-01 and DM-03

6.4.3 DM-05/07

Finally, the same tensile and electrical tests were carried out on samples DM-05 and DM-07, which were cut from the same 3-meter conductor fabricated using Assembly Method 3 — the most recent and reproducible process.
Sample DM-05 was tested first. It was initially loaded up to 0.4% strain, then subjected to further tests in 0.05% strain increments until full degradation occurred.

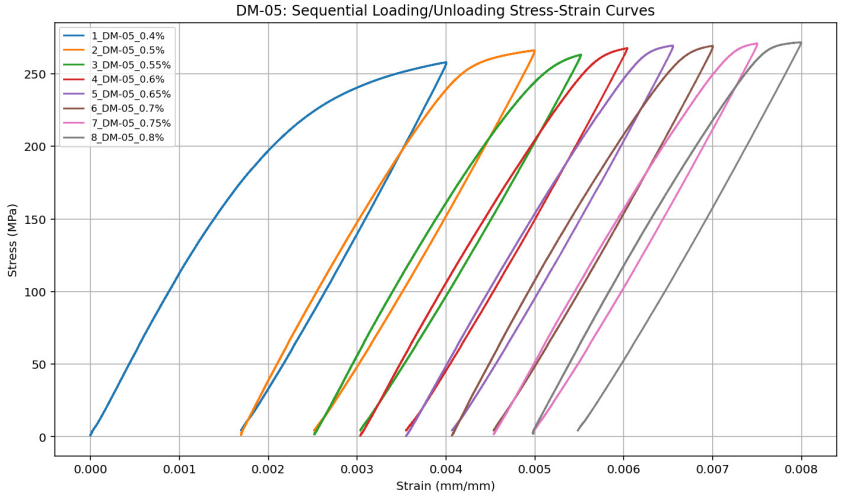

Figure 6.10: Tensile cycles - Stress-strain curve for DM-05

As shown in the stress-strain diagram, the elastic limit is around 260 MPa, with

no significant changes in material behavior due to strain hardening between the various tests.
The plots below show the electrical results obtained after each tensile cycle, as well as a comparison with DM-07 — once again confirming the reproducibility of this manufacturing process.

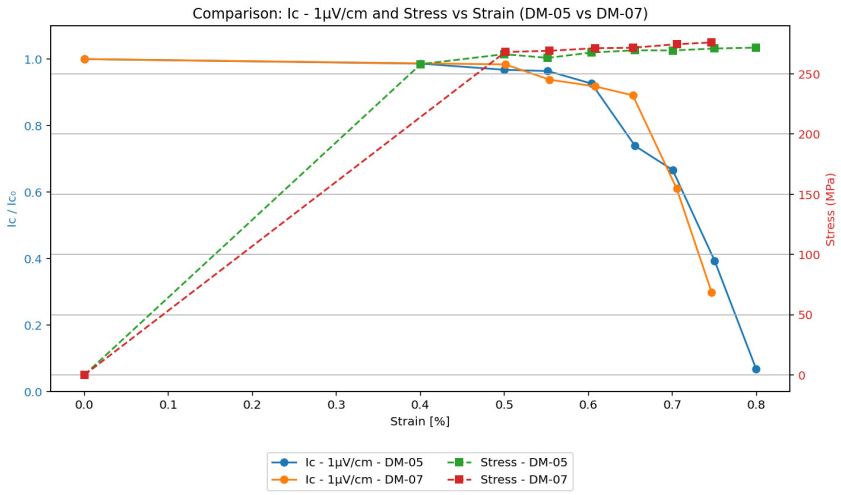

Figure 6.11: Comparison of normalized critical current vs. strain: DM-05 vs DM-07

Comparison between DM-05 and DM-03

Although Assembly Methods 2 and 3 are nearly identical, the mechanical test results reveal significant differences.
The sample manufactured with Method 3 shows higher mechanical strength (with a higher yield stress) and greater ability to retain superconducting properties at higher strain levels.
The main difference between the two methods lies in the handling of the copper flattening process. In Method 2, the lack of a guide during rolling resulted in excessive deformation and a non-uniform cross-section along the sample length.

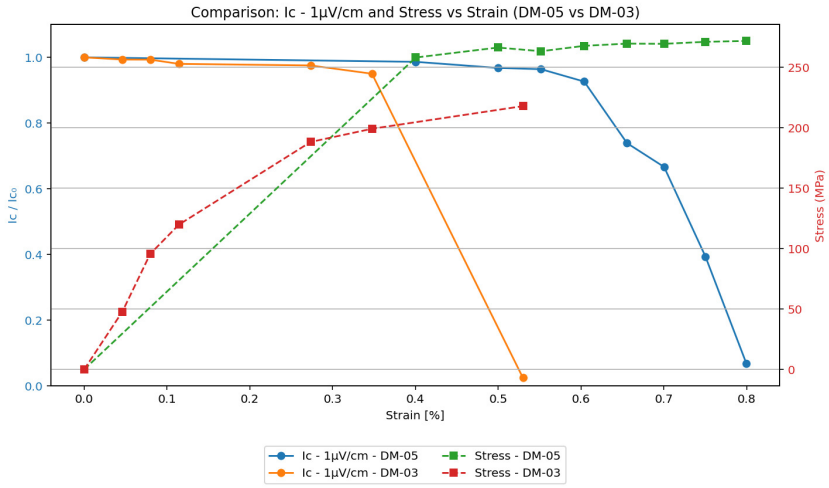

Figure 6.12: Mechanical and electrical comparison between DM-05 and DM-03

6.4.4 DM-06/08

A different procedure was adopted for samples DM-06, in which repeated loading cycles at constant maximum strain were applied. The aim was to investigate whether this kind of loading could lead to premature degradation or if it would have no impact on the conductor's properties.

Sample DM-06 was subjected to 50 load–unload cycles at 0.3% strain, followed by an almost complete unloading. Unfortunately, this test was interrupted due to a failure in one of the O-loops used to secure the extensometer to the conductor. This caused incorrect strain measurements. However, the test was halted promptly, likely preventing overloading of the sample.

Analysis of Stress-Displacement Curves and Strain Estimation
In order to analyze data from these failed tests (where the extensometer was unreliable), we focused on the displacement values provided by the testing machine, which are independent of extensometer errors. The goal was to find a correlation between machine displacement and actual strain.

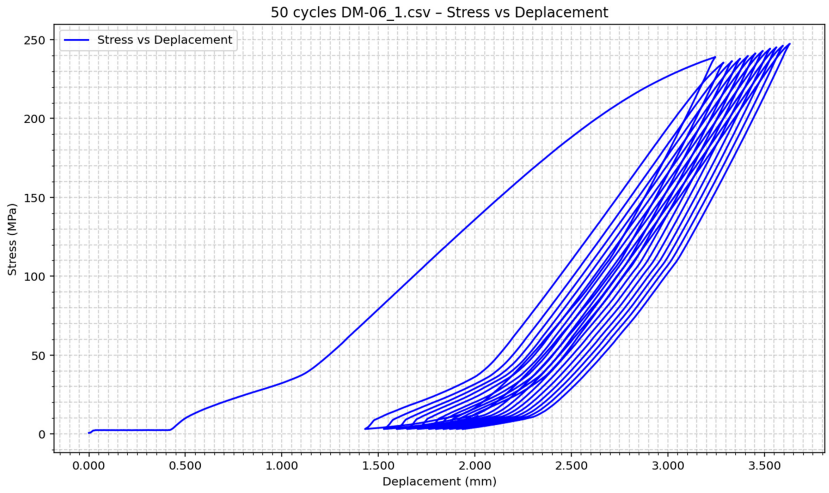

Figure 6.13: Stress-displacement curve for DM-06. Objective: 50 load-unload cycles at constant strain. Test interrupted at cycle 11.

Upon reviewing the stress-displacement curves, we observed key differences compared to standard stress-strain plots, including:

- The initial portion of the curve often appears as a horizontal line. This is attributed to the settling and alignment of the machine components, during which no significant stress is applied to the sample.
- The slope of the loading curve is not constant throughout the cycle, likely due to ongoing adjustments within the test setup.
- During unloading, the stress-displacement curve deviates from linearity, particularly at low stress values. This shift — where displacement increases more than expected for a given stress drop — may be caused by nonlinear effects such as material relaxation, hysteresis, or residual deformation.

Due to these deviations, it was decided to focus only on the peak values of each load cycle (maximum and minimum), which are less affected by machine settling. Two main methods were evaluated for estimating strain from displacement data.

Approximation Method

This method used data from samples DM-05 and DM-07, which were derived from the same initial conductor and thus share mechanical properties.
Stress-displacement plots from individual tests were analyzed to determine the initial offset in displacement (caused by machine settling), which was subtracted

from the maximum displacement point.
Since all tests reached strains close to 0.3%, and the initial part of the curve is unreliable, the following steps were adopted:

1. Determine the machine displacement corresponding to 0.2% and 0.3% strain.

2. Compute the difference between these values, defined as the "delta displacement", the displacement required to increase strain by 0.1%.

The average values of the displacement for 0.2% strain and for the 0.1% increment were then calculated across all tests.

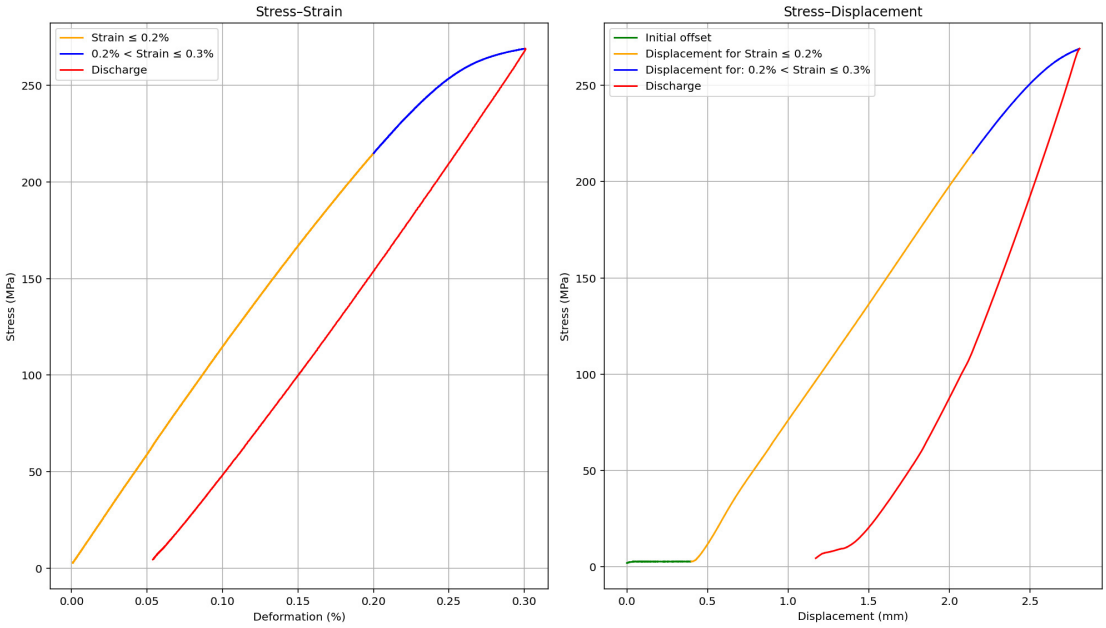

Figure 6.14: Example of the application of the approximation method on a properly conducted traction test. In green (second graph), the offset due to machine displacement is shown and subtracted. The yellow zone highlights the strain region up to 0.2%. The blue segment represents the "delta displacement" used to evaluate the relationship between strain and displacement. The red area indicates the unloading phase.

The procedure to estimate strain from a measured displacement is as follows:

1. Identify the maximum stress point and record its displacement.

2. Subtract the initial offset.

3. Subtract the average displacement value for 0.2% strain.

4. Multiply the remaining value by 0.1 and divide by the delta displacement.

5. Add 0.2% to obtain the final strain value.

The formula used is given in equation (6.1). The method was validated by applying it inversely to DM-05 and DM-07 data to check for consistency.

$$\text{Strain}(\%) = \frac{(\text{Depl}_{\text{tot}}\,[\text{mm}] - \text{Offset}\,[\text{mm}] - \text{Depl}_{0.2\%}\,[\text{mm}]) \cdot 0.1\%}{\Delta\text{Displacement}\,[\text{mm}]} + 0.2\% \quad (6.1)$$

While many results obtained with this method were consistent with actual strain values, some outliers exhibited significant deviations, prompting the development of an alternative approach for cross-validation.

Linear Relationship Method

This second method uses the **unloading** portion of a successful tensile test to derive a linear relationship between strain and displacement, exploiting the most linear region of the stress-strain curve.
The start and end points of this linear unloading segment were used to calculate deltas for: force (kN), strain (%), and displacement (mm). This automatically excludes initial machine settling effects. The analysis uses the following relation:

$$\Delta L_{\text{tot}} = \Delta L_{\text{sample}} + k \cdot \Delta F \quad (6.2)$$

Here, ΔL_{tot} is the total machine displacement, including both sample elongation and press deformation. The second term accounts for the latter using a correction factor k (included for completeness, though often negligible).

The formula is rewritten as:

$$\Delta Displacement = \Delta\varepsilon \cdot L_0 + k \cdot \Delta F \quad (6.3)$$

And solving for k:

$$k = \frac{\Delta Displacement - \Delta\varepsilon \cdot L_0}{\Delta F} \quad (6.4)$$

This k factor was calculated from DM-05 and DM-07 test data to obtain an average value for use in inverse analysis.
This method proved more reliable, with maximum deviations of 3.8% compared to known strain values.

To reanalyze the faulty test using this method, two characteristic points were selected: the first and the last visible peaks in the tensile loading cycles, corresponding approximately to the beginning and end of the plastic transition (see figure 9.7).
For each of these two points, the force and machine displacement were extracted. Their differences (ΔF and ΔDisplacement) were then used in the following formula to calculate the corresponding strain increment:

$$\Delta\varepsilon = \frac{\Delta\text{Displacement} - k \cdot \Delta F}{L_0} \tag{6.5}$$

This value represents the estimated strain accumulated between the two selected peaks. It was added to the strain estimated at the first peak, obtained via interpolation from validated tests, to reconstruct the total strain applied during the faulty test.

The main difficulty of this method lies in the interpolation of the strain corresponding to the first peak: due to the variability among tests, similar strain values can correspond to slightly different displacement values.

Comparison of Methods

Both methods were applied to analyze the results of DM-06 in order to verify consistency.

Both methods produced consistent strain estimates around 0.44%, and no electrical degradation was observed. This allowed testing to continue under controlled conditions with no further issues.

Obtained Results

Only the first traction test was affected by a measurement error. All subsequent tests were successful, allowing not only continued cycling at the same final strain level but also an increase in maximum strain to assess the critical threshold.

The initial tests confirmed the conductor's ability to withstand repeated tensile cycling at a constant strain of approximately 0.4%, prompting an increase in the maximum target strain. Test 5 was conducted at a target of 0.5% strain. Since no degradation in superconducting properties was observed, test 6 pushed the strain to 0.64%, resulting in complete loss of superconductivity.
Comparing this result with single-load tests performed on DM-05 and DM-07 (samples originating from the same initial conductor, thus with identical properties), it is evident that cyclic loading leads to more rapid degradation. At 0.65% strain,

Test #	Cycles per Test	Total Cycles	Max Strain (%)
1	10	10	0.438
2	40	50	0.430
3	50	100	0.407
4	100	200	0.394
5	100	300	0.501
6	100	400	0.643

Table 6.1: DM-06 traction cycle test results

only a partial loss (approximately 30%) of the critical current is typically expected, whereas DM-06 exhibited an 80% loss in I_c under cyclic loading.
On the other hand, the outcome at 0.5% strain is encouraging: no degradation was observed despite 300 load cycles, suggesting a safe operating margin for this conductor configuration.

6.4.5 Summary of Results

From the tensile tests performed on the various samples, the following conclusions can be drawn:

- The testing procedure is repeatable, and the assembled conductor retains consistent properties along its entire length.
- The assembly process significantly influences the conductor's mechanical behavior under tension. Ensuring its repeatability is crucial to achieving consistent performance.
- Tensile cycling does not lead to a loss of superconducting properties up to 0.5% strain. However, degradation of I_c becomes significantly more rapid beyond the 0.6% threshold.

Assembly process 3 (selected as the optimal configuration) allows for near-complete retention of the critical current value (less than 10% degradation) at strains up to 0.6%. Furthermore, the loss of superconducting properties is not abrupt: partial properties are retained up to 0.8% strain. This outcome aligns with the literature findings presented in Section 5.1, confirming that no significant degradation of the superconducting tape occurs during the assembly phases.
In conclusion, assembly process 3 enables the production of longer conductors, with shorter manufacturing times, improved mechanical performance, and good reproducibility.

Chapter 7

Compression tests

The second mechanical test performed to characterize our conductor was the compression test.
Compression tests are fundamental mechanical tests used to evaluate the behavior of a material under compressive loads. During the test, a sample is compressed between two flat surfaces while the applied force and the resulting deformation are recorded.

7.1 Literature on compression tests on HTS tapes

Several studies have investigated the effects of transverse mechanical loading on REBCO and other HTS tapes[19]. In particular, tests performed on tapes with different copper layer thicknesses (40, 100, and 110 μm, and without Cu layer) have shown that the copper stabilizer plays a crucial role in determining the mechanical response under transverse compression.

Experimental results demonstrated a clear correlation between copper layer thickness and the force level at which critical current (I_c) degradation begins. Specifically, the critical force decreased with increasing copper thickness. The tape without a copper layer showed no measurable I_c degradation even under forces up to 3.5 kN.

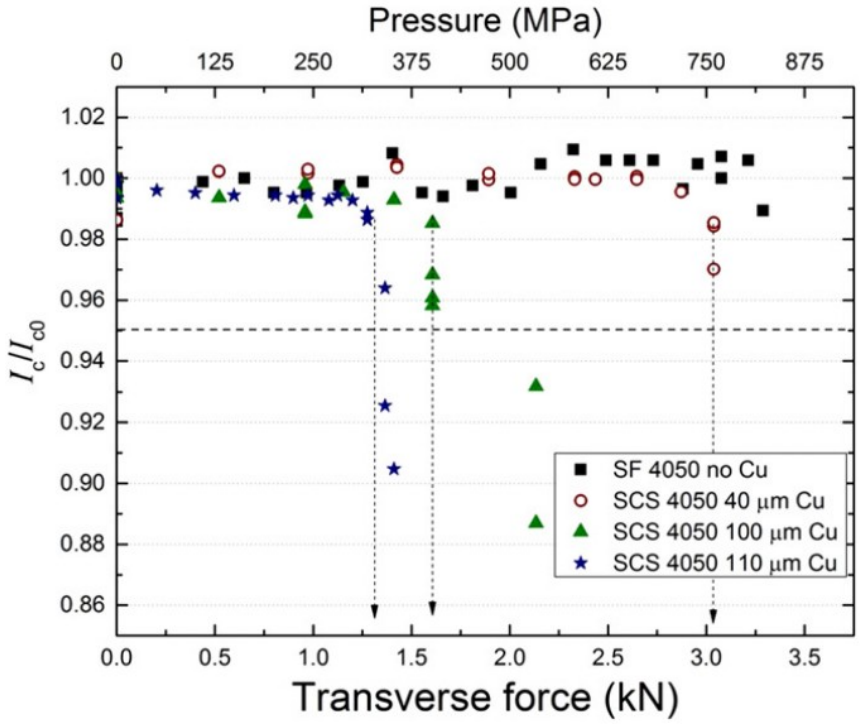

Figure 7.1: I_c/I_{c0} as a function of applied force (and average pressure) for tapes with different Cu layer thicknesses.[19]

These findings highlight the strong influence of the copper layer's geometry and mechanical properties on the electromechanical stability of HTS tapes under transverse stress.

For this reason, it is important to verify whether the addition of copper plates through the assembly process may lead to a reduction in transverse compression strength. However, it should be noted that in commercial HTS tapes, the copper is typically applied by electroplating, whereas in our conductor it is joined through a brazing process using a heating device. Therefore, the same impact on the mechanical properties is not expected.

7.2 Test procedure

The compression tests were carried out using the same press employed for the tensile tests described earlier. Instead of the tensile grips, two circular plates were mounted at the top and bottom of the press. Two strain gauges were initially

placed between these plates to measure deformation at opposite points, thereby verifying the uniformity of the applied force on the sample.

To perform this verification, preliminary tests were conducted using copper. However, results showed a degree of asymmetry in the strain measurements between the two strain gauges, likely due to imperfect flatness of the compression plates. Therefore, the strain gauges were removed, and uniformity was assessed using Fujifilm Prescale film, which provides a visual indication of the stress distribution—intensifying in color at areas subjected to higher pressure.

This method allowed for a qualitative visual check of stress distribution. The first test clearly revealed non-uniformity, with stress concentrations observed at the center and at the edges. Consequently, a thin Teflon sheet was inserted on both sides of the conductor to improve stress distribution. This solution proved effective, resulting in a much more uniform stress profile.

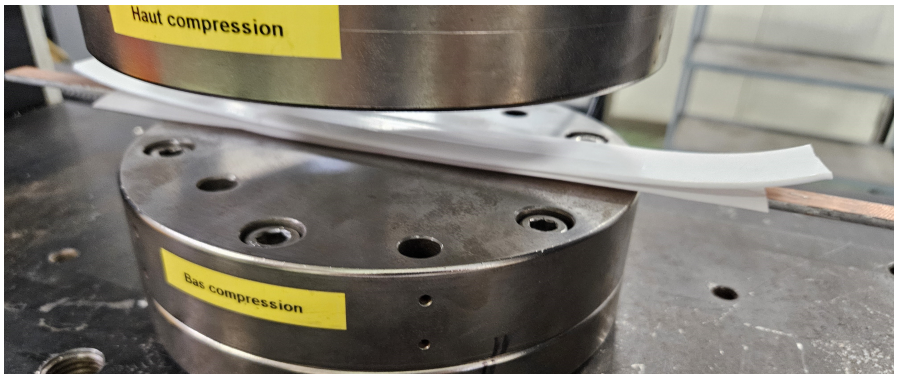

Figure 7.2: Compression test setup with Teflon sheets on both sides.

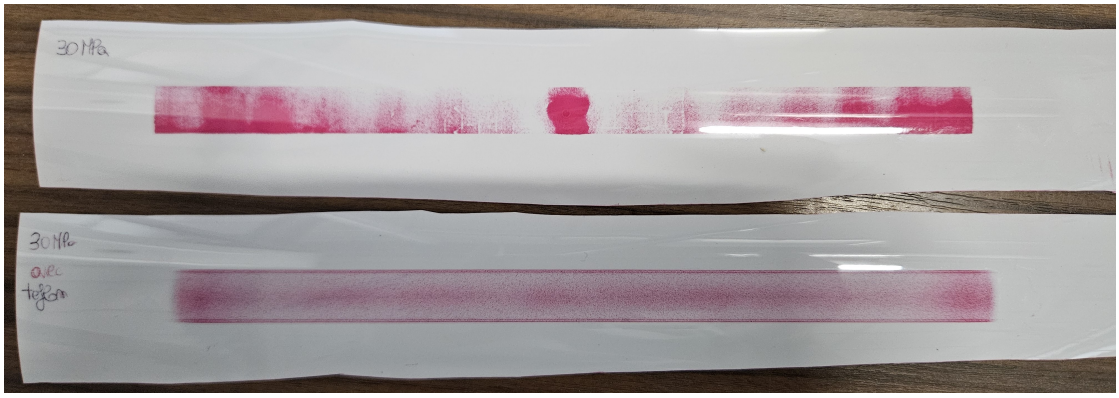

Figure 7.3: Fujifilm Prescale film results. Top: without Teflon. Bottom: with Teflon sheets.

Another limitation to consider is the maximum force allowed by the press. Given that the plates have a diameter of approximately 20 cm and the conductor under test has a surface area of 12 mm in width, the total compressed area is approximately 2400 mm^2. With a maximum press load of 300 kN, this configuration would not allow stress levels beyond 125 MPa. Additionally, to ensure safe operation, it is advisable to stay below the system's load limit. The chosen solution was to reduce the contact area under compression.

To do so, a copper plate with the same width as the conductor (12 mm) and a length of 5 cm was used. The resulting test stack configuration was as follows:

Figure 7.4: Setup for compression tests. Grey: press plates. Red: 5 cm copper plate. Yellow: conductor under test. Blue: teflon.

Prescale film was continuously used to verify the uniformity of stress distribution.

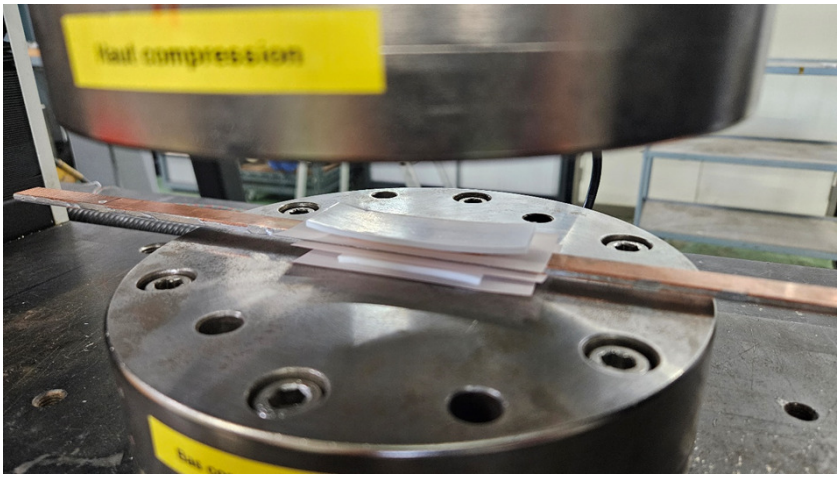

Figure 7.5: Compression setup with reduced length (5 cm).

Figure 7.6: Side view of stacked elements. Prescale film was inserted between all layers to detect stress variations.

This setup allowed high-stress compression tests to be conducted. However, due to the presence of Teflon sheets, strain gauges could not be used, preventing acquisition of full stress–strain curves. Therefore, tests were conducted based on the applied force rather than resulting deformation. Electrical measurements were performed after each mechanical test, and the applied load was increased progressively.

A key technical challenge was the precise and repeatable positioning of all components in the stack to ensure proper alignment and consistent placement on the conductor between tests. During the electrical tests, the central voltage taps (U2) were placed within the compressed area, while the outer pair of pogo pins remained outside.
The conductor was also positioned as centrally as possible throughout all tests.

During the 200 MPa test, the Teflon sheets ruptured. As a result, the test had to be repeated using a 5 cm copper plate also on the bottom side to ensure that the stress was applied only within the target region. The final test configuration is shown in the figure below:

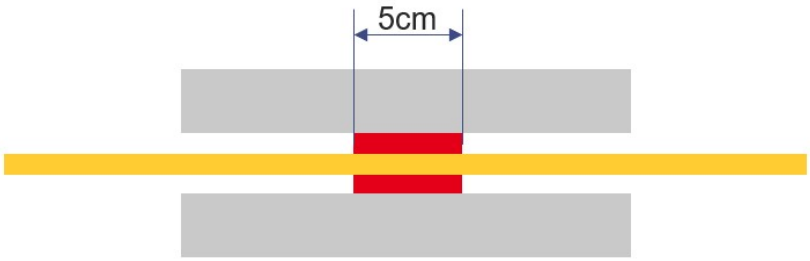

Figure 7.7: Final setup for compression tests at 200 MPa and above. Grey: press plates. Red: 5 cm copper plates. Yellow: conductor under test.

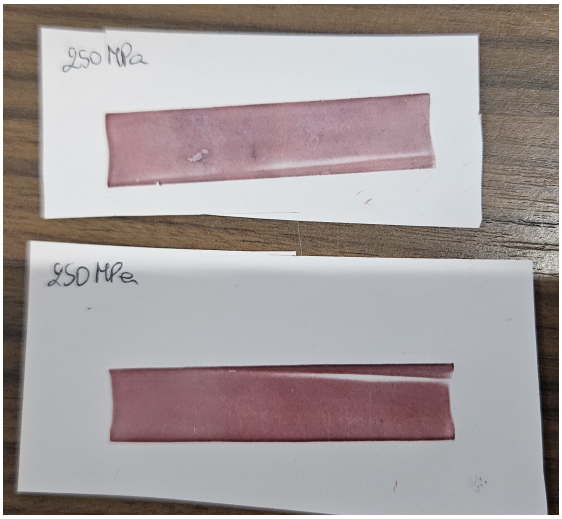

Figure 7.8: Stress distribution after compression test at 250 MPa.

Figure 7.9: Rupture of the Teflon sheet following the 200 MPa compression test.

7.3 Results

Several compression tests were performed on sample DM-09, assembled using process 3. The initial tests were conducted at low stress levels to verify the reliability and repeatability of the procedure. Stress was then increased in 50 MPa increments, starting from 50 MPa and going up to 300 MPa.

The results are summarized in the graph below, which shows the normalized critical current as a function of applied compressive stress:

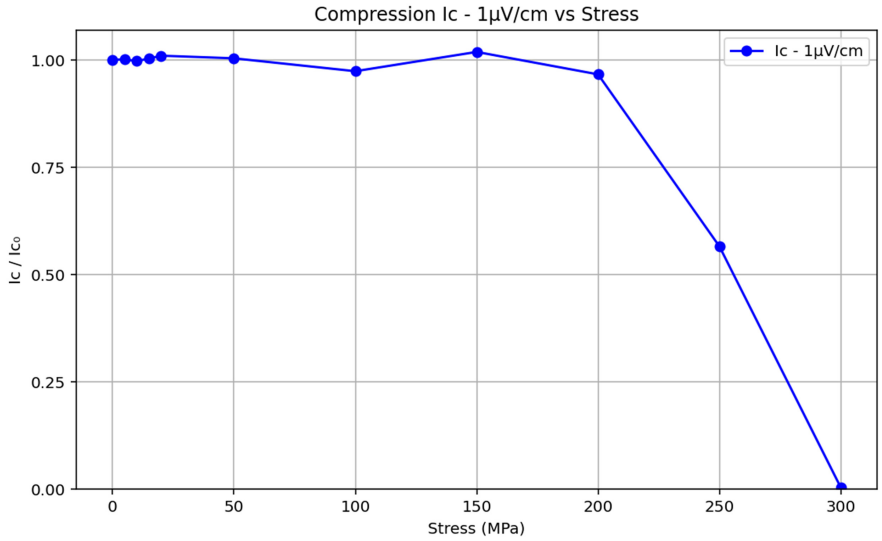

Figure 7.10: Normalized I_c vs. compressive stress for sample DM-09.

No degradation was observed up to 200 MPa. However, at 250 MPa a loss in I_c exceeding 40% was recorded, followed by a complete loss of superconducting properties at 300 MPa.

These results are encouraging when compared with the data reported in the literature, indicating that the addition of copper plates during the assembly process does not lead to increased sensitivity to transverse compressive stress. On the contrary, the conductor exhibits a comparable or even improved mechanical robustness, confirming the effectiveness of the adopted assembly technique.

Chapter 8

Bending tests

Bending tests are particularly necessary for conductors as they must ensure the preservation of superconducting properties after the winding process for the solenoid assembly.

8.1 Literature on bending tests on HTS tapes

To select the critical radius value for performing the tests, a literature review was conducted on the behavior of individual REBCO tapes under bending [20]. The values considered in this publication refer to SST tapes, as they are from the same manufacturer as those used for assembling our conductors.

When a REBCO tape is subjected to bending, the superconducting layer experiences either tensile or compressive strain depending on whether it is on the outer or inner side of the curvature.
The bending strain can be expressed as:

$$\varepsilon_b = \frac{y}{\rho} \tag{8.1}$$

where y represents the distance between the REBCO layer and the neutral axis, and ρ is the bending radius.

The position of the neutral axis can be determined based on the mechanical properties and geometry of the various layers composing the tape:

$$y_{\text{neutral}} = \frac{t}{2} - \frac{\sum_i E_i \gamma_i \frac{t_i}{2}}{\sum_i E_i t_i} \tag{8.2}$$

where:

- t is the total tape thickness;

- t_i is the thickness of each layer;
- E_i is the elastic modulus of each layer;
- γ_i are parameters related to the position and thickness of each layer.

Based on this formulation, the neutral axis position was calculated, finding that it was displaced by only about 2 μm from the tape's geometric center. This deviation results in a difference of approximately 0.02% in the calculated strain value and can therefore be considered negligible.

Consequently, the neutral axis can be approximated as the tape's geometric center. Therefore, in this work, the bending strain is calculated using Equation (8.1), replacing y with the distance between the REBCO layer and the tape's geometric center.

As a result of this study [20], the limit radius values were obtained:

- Compressive state: ε = -0.41%
- Tensile state: ε = 0.3%

Once these values were obtained, they need to be adapted to our geometry. The value of y in Equation (8.1) will be given by the distance of the REBCO layer relative to the conductor center.
Since metallographic analysis images were not yet available when these calculations were performed, the thickness of the solder layer between the two REBCO tapes was neglected. The thicknesses of the individual layers shown in the figure below were obtained from the datasheet provided by the REBCO tape manufacturer.

Figure 8.1: Schematic representation of the REBCO layers within the SST tape. The dashed line at the top represents the geometric center of the conductor. The REBCO layer is highlighted in red.

Through this structure, it is possible to determine the distance y of our conductor, which will be approximately 23 μm.

Considering the strain limits in the compressive state obtained from tests on individual tapes, we can establish that the bending radii should be:

- Compression state: 5.5 mm;
- Tensile state: 8 mm.

Safety margins must then be added to these values due to possible copper delamination effects, which could lead to a faster loss of superconducting properties.

In fact, tests performed in parallel on the same type of conductor showed partial degradation of the critical current already on windings with a 120 mm diameter. For this reason, the operational approach was changed, and bending tests were performed with similar diameter values. Tests were carried out for diameters of 150, 120, and 100 mm.

8.2 Test procedure

To perform this type of test, it was necessary to develop a technique to bend the conductor to the desired diameter and also adapt the test bench to measure the critical current when the conductor is not flat.
3D-printed pieces were chosen to allow manual bending of the conductor along a semicircle that ensured it remained in position. Additionally, small lateral blocks could be screwed in to prevent the conductor from opening.

Figure 8.2: Process to achieve bending of the conductor. One end is clamped in a bench vise while the other is manually bent to adhere to the 3D-printed piece (in black).

The test bench for measuring the critical current in liquid nitrogen was modified in the following configuration:

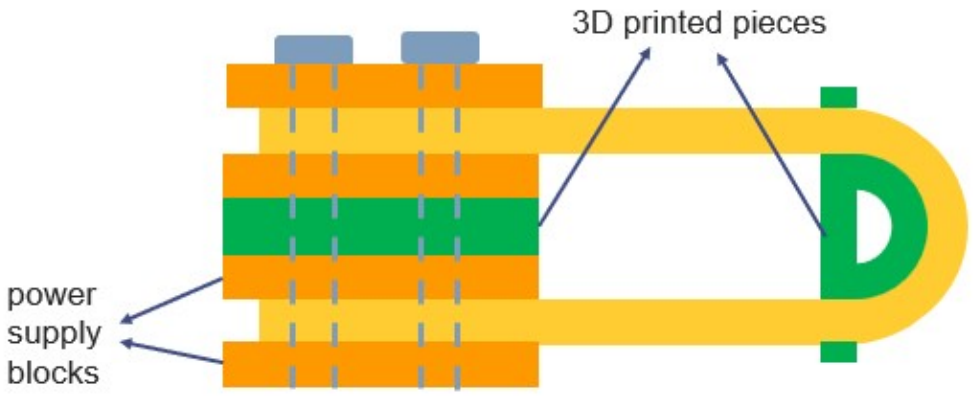

Figure 8.3: Schematic of the bending test bench setup. The conductor is shown in yellow, the copper blocks for current supply in orange, the 3D-printed components in green, and the screws securing the structure in gray.

With this configuration, the two ends of the conductor can be stacked vertically using the same blocks used for the current supply in previous tests. Some drilled 3D-printed blocks were placed between the supply blocks to maintain the structure at the exact bending diameter. Finally, long screws passing through the entire structure were used to secure everything.
Since pogo pins could not be used in this configuration, potential taps were soldered directly onto the surface of the conductor in the region subjected to bending. A tin-indium solder alloy with a lower melting point than the alloy used in the conductor assembly was employed.

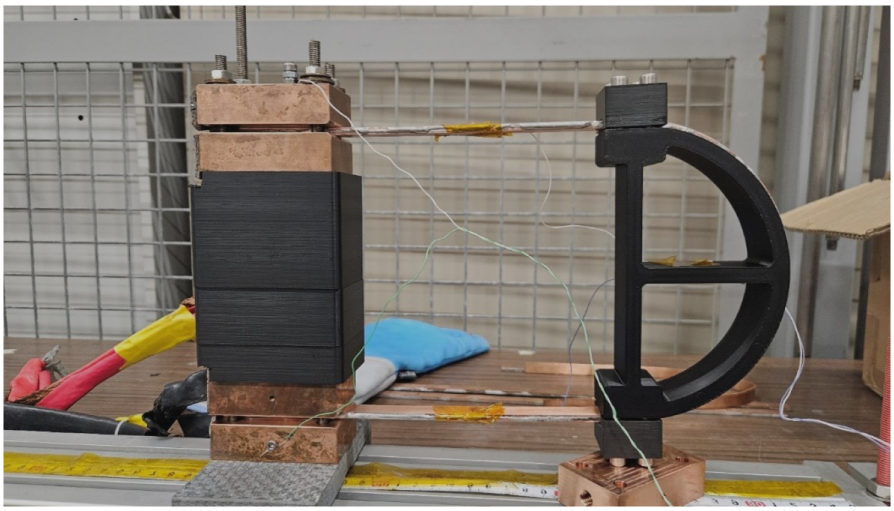

Figure 8.4: Electrical test setup for a conductor bent to a 150 mm diameter.

Since a conductor subjected to bending cannot be reused for subsequent tests at different diameters, three samples were used:

- DM-12: length 69 cm, bending diameter 150 mm;
- DM-13: length 62 cm, bending diameter 120 mm;
- DM-14: length 56 cm, bending diameter 100 mm.

8.3 Results

The results of the three tests performed showed no loss in the critical current value compared to the measurement taken before bending.
The assembled conductor should not experience any reduction in I_c under operational conditions. This result therefore suggests that the loss of superconducting properties observed in the winding tests is likely not due to the bending effect, and an alternative cause will need to be investigated.
Moreover, although a critical diameter was not determined, these tests allowed the development of a methodology applicable for future tests in which it will be possible to further reduce the bending diameter.

Chapter 9

Torsion tests

9.1 Literature on torsion tests on HTS tapes

The last type of test performed on the conductors during the internship was the torsion test. The objective, once again, was to determine the strain limits that cause the loss of superconducting properties of our conductor.
In order to estimate these limits, a literature review on tensile tests performed on individual HTS tapes was conducted.

According to a reviewed publication[21], the 4 mm wide SuperPower REBCO tape is able to maintain its superconducting properties up to a twist pitch of 4.34°/mm.
The same study attempted to establish a relationship between torsional strain and uniaxial tensile strain, allowing comparison with tensile tests or the possibility of performing combined torsion-tension tests.
Since torsional strain is non-uniform across the tape width, with maximum stress at the edges and minimum at the center, the focus is placed solely on the maximum stress value.

The following relationship was used:

$$\varepsilon_L = \frac{\theta^2 \left(x^2 - \frac{w^2}{12}\right)}{2} \tag{9.1}$$

where:

- ε_L is the equivalent tensile strain;
- θ is the twist pitch in rad/mm;
- x is the horizontal distance from the tape center (across the width) in mm;

- w is the total tape width in mm.

From this, the maximum strain can be derived as:

$$\varepsilon_{L,\max} = \frac{\theta^2 w^2}{12} \tag{9.2}$$

A second publication[19] was also reviewed, providing different results for tensile tests performed on the same REBCO tape model.

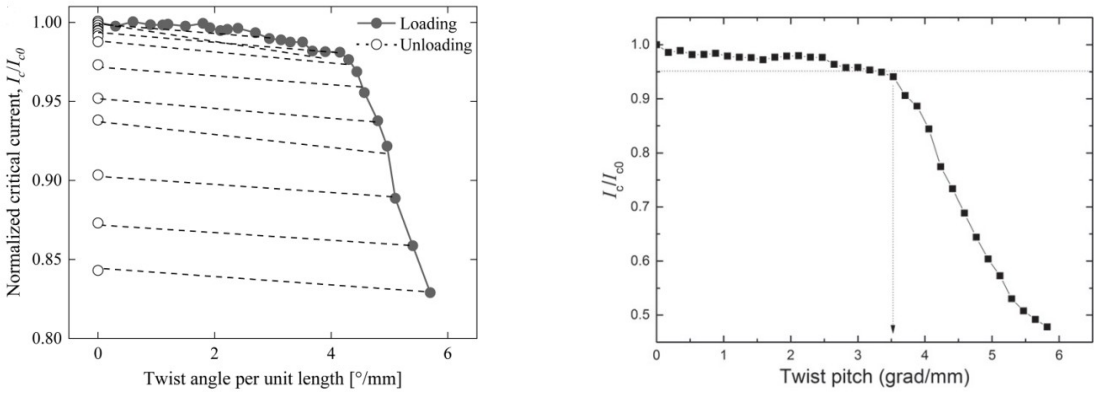

(a) Ic/Ic0 as a function of the twist pitch (loading–unloading cycles).[21]

(b) Normalized critical current as a function of the twist pitch.[19]

Figure 9.1: Torsion test results on single REBCO tapes. Comparison of two different research studies.

Using the relationship in (9.2), it is possible to adapt the limit values from the literature to our sample, which has a larger width (12 mm), in order to determine the twist pitch to be applied to our conductor.

	θ (4 mm tape)	ε_L	θ (12 mm tape)
Research 1	4.34°/mm	0.765%	1.446°/mm
Research 2	3.5°/mm	0.497%	1.167°/mm

Table 9.1: Comparison of torsion angles θ and longitudinal strains ε_L measured for 4 mm and 12 mm tapes in two studies, with twist pitches adapted to the geometry of our conductor.

Based on these data, the procedure for performing the tests was developed, taking into account that the available samples were numerically limited and had a total length of 40 cm, of which a portion was unusable because it was clamped

between the copper blocks for electrical feeding during the tests.
Furthermore, for practical reasons, it was preferable to use torsion angles in multiples of 180° to keep the conductor flat and suitable for the geometry of the available test bench.
For this reason, since the torsion angle could not be varied freely, the length subjected to torsion was adjusted in order to achieve different twist pitch values.

9.2 Test procedure

The torsion tests were performed manually due to the absence of a dedicated machine.
Particular attention was paid to clamping the sample at both ends before applying torsion; this allowed limiting the deformation to the selected section length (which affects the twist pitch), thereby avoiding deformation of the ends.

The conductor was clamped at one end in a bench vise, while the other end was secured using two aluminum blocks screwed together. In this way, using pliers, it was possible to apply the force on the aluminum component to achieve the desired torsion.

Figure 9.2: Conductor clamped at both ends in a bench vise and aluminum blocks before applying torsion.

Figure 9.3: Conductor after applying a 360° on a 20cm long section.

The length subjected to torsion was measured in advance in the central region to optimally position it between the two clamping elements.

Once this procedure was completed, the conductor could be mounted on the test bench. By securing it between the copper blocks, it was ensured that the conductor remained completely flat, allowing the placement of the potential taps. These taps were positioned at the ends of the region actually subjected to mechanical stress.

Figure 9.4: Top view of the test bench setup showing the conductor fixed between the copper blocks (180° torsion on a 20cm long section).

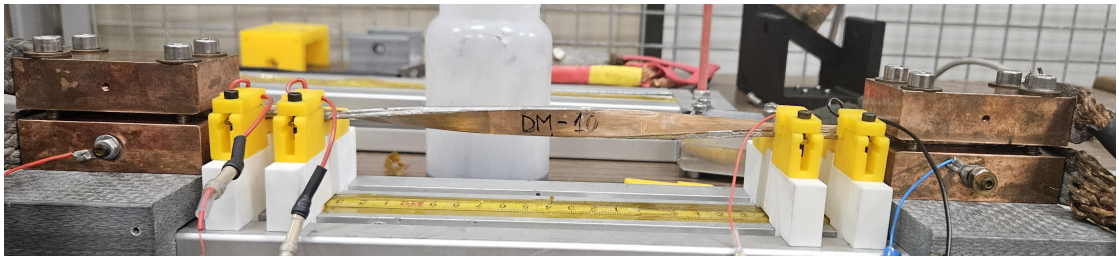

Figure 9.5: Front view of the test bench setup with the conductor positioned between the copper blocks for potential lead placement (180° torsion on a 20cm long section).

The conductors used for this test were DM-04 and DM-10. The test configurations performed are summarized in the following table:

Sample	**Length of twisted section (mm)**	**Angle (°)**	**Twist pitch (°/mm)**	ε_L **max (%)**
DM-10	200	180	0.9	0.3
DM-04	150	180	1.2	0.5
DM-10	200	360	1.8	1.18

Table 9.2: Summary of torsion test parameters.

9.3 Results

The results of the torsion tests were plotted showing the relationship between the normalized critical current and the twist pitch, as well as the equivalent tensile strain calculated using equation (9.2).

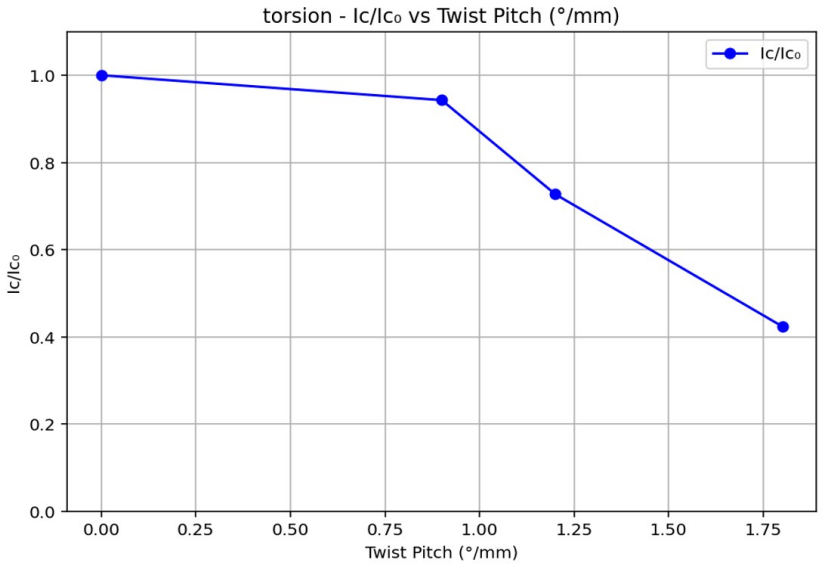

Figure 9.6: Normalized critical current of the conductor as a function of the twist pitch.

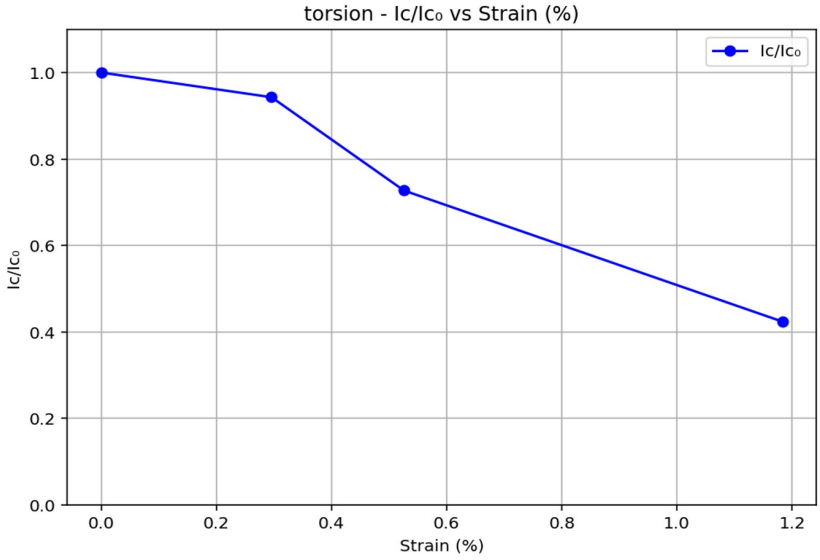

Figure 9.7: Normalized critical current of the conductor as a function of the maximum equivalent tensile strain.

From the obtained results, it can be observed that the loss of superconducting properties begins at lower values compared to the literature data shown in Table 9.1. In fact, our sample exhibits a partial loss at a twist pitch of 0.9°/mm, which is lower than the range between 1.16°/mm and 1.40°/mm reported for individual REBCO tapes. Several factors may influence this behavior: firstly, the REBCO tape considered in the literature is not from the same manufacturer as the one used in our conductor; additionally, possible degradation of the tape during the assembly process, as well as delamination phenomena during torsion, must be taken into account.

The behavior of the curve in Figure 9.6 is also noteworthy, as it shows a more gradual decrease of the critical current with twist pitch compared to the previously shown literature graphs in Figure 9.1.

Chapter 10

Thermal Stress Analysis

In the conductor under study, the REBCO tape is bonded to copper layers in order to improve the electrical stability and thermal conduction capability of the system. However, these two materials exhibit different coefficients of thermal expansion.

When the composite is subjected to temperature variations, copper and the REBCO tape tend to expand or contract by different amounts. Since they are rigidly bonded, they cannot deform freely, and this mismatch generates internal thermal stresses within the conductor.

These stresses manifest as tensile or compressive stresses in the different components, depending on the direction of the thermal change and the properties of each material. Consequently, the REBCO tape may already experience a state of mechanical pre-stress before any external loads are applied.

The presence of these thermal stresses is therefore an important aspect to consider when interpreting the results of mechanical tests performed on the conductor. Indeed, they can alter the actual stress state of the REBCO tape and, as a result, affect the representativeness of the tests relative to real operating conditions.

Interest in this type of evaluation lies in the possibility of comparing the mechanical test results obtained on the conductor with those reported in the literature for individual REBCO tapes. This allows verification of whether the measured performance of the conductor truly reflects the intrinsic behavior of the REBCO tape or if it is influenced by thermal stresses induced during assembly.

Moreover, having an estimate of the actual stress in the REBCO tape enables comparison of different manufacturing or assembly processes, in which thermal stresses may vary depending on the materials used or the bonding techniques

adopted.

Since the overall contraction of the conductor depends on the properties of its components, its total deformation can be quantified through a force equilibrium:

$$E_{\mathrm{Cu}}(\varepsilon - \varepsilon_{\mathrm{Cu}})A_{\mathrm{Cu}} + E_{\mathrm{REBCO}}(\varepsilon - \varepsilon_{\mathrm{REBCO}})A_{\mathrm{REBCO}} = 0 \tag{10.1}$$

where:

- E_{Cu} and E_{REBCO} are the Young's moduli of copper (Cu) and REBCO, respectively, accounting for the mechanical properties of the two materials.
- A_{Cu} and A_{REBCO} are the cross-sectional areas of the two components, used to calculate the internal forces.
- $\varepsilon_{\mathrm{Cu}}$ and $\varepsilon_{\mathrm{REBCO}}$ are the free (or "natural") strains of the two materials, i.e., the strains they would experience if isolated.
- ε is the overall strain of the composite conductor, resulting from the mechanical equilibrium between the two layers.

Since the conductor's cross-section is primarily composed of copper, its effect will dominate over that of the REBCO tape within the overall equilibrium. Determining the mechanical and geometric properties, we obtain:

$$A_{\mathrm{REBCO}} = \text{width} \times \text{thickness} \times \text{n}^\circ \text{ of tapes} = 12 \text{ mm} \times 0.095 \text{ mm} \times 2 = 2.28 \text{ mm}^2$$

$$A_{\mathrm{Cu}} = \text{width} \times \text{thickness} \times \text{n}^\circ \text{ of plates} = 12 \text{ mm} \times 2 \text{ mm} \times 2 = 48 \text{ mm}^2$$

Regarding the evaluation of the Young's modulus of copper, the value obtained from tensile tests on individual copper plates was used, resulting in a value of **112 GPa**.
Since the same tests could not be performed on individual REBCO tapes, the Young's modulus was estimated from the main constituent materials reported in the literature. The two copper layers within the tape have a total thickness of 40 μm, while the Hastelloy layer is 50 μm thick. Performing a weighted average of these properties yields a Young's modulus of **159.4 GPa**, consistent with typical values reported for REBCO in the literature.

The main phenomena that generate thermal stresses during our tests are given by:

- Assembly process;
- Electrical tests in liquid nitrogen.

10.1 Assembly process

As discussed in Chapter 3, to obtain the final conductor it is necessary to heat the components to allow the solder material to melt and bond the REBCO tape to the copper.

During this heating phase, the expansion of the individual components can be considered independently, so each element undergoes expansion proportional to its thermal expansion coefficient. However, during the cooling phase, due to the solidification of the tin-lead alloy, the REBCO tape and copper are forced to contract together. Since copper has a higher thermal expansion coefficient, it can be expected to be under tension in the final conductor, while the REBCO tape will be in compression.

The temperature range to be examined therefore spans from the melting point of the solder material (453 K) down to room temperature (293 K).

The next step is to determine the values of $\varepsilon_{\mathrm{Cu}}$ and $\varepsilon_{\mathrm{REBCO}}$ in order to apply equation (10.1).
For copper, the properties are readily available in the literature[22], which provides thermal expansion coefficients at various temperatures. To estimate the total strain, the available data were first interpolated to determine the expansion coefficients at the two ends of the temperature range considered (293 K and 453 K).

Next, the total thermal strain was calculated using the following relation:

$$\varepsilon = \sum_{i=1}^{n} \left(\frac{\alpha_i + \alpha_{i+1}}{2} \right) \cdot (T_{i+1} - T_i)$$

This expression allows the total strain ε to be estimated as the sum of the incremental expansion contributions over each temperature interval. Since the thermal expansion coefficient α varies with temperature, the total range is divided into n subintervals $[T_i, T_{i+1}]$, within which the variation of α is assumed approximately linear.

In this formulation:

- α_i and α_{i+1} are the thermal expansion coefficients at the two ends of the interval $[T_i, T_{i+1}]$;
- $T_{i+1} - T_i$ is the width of the temperature interval;
- $\frac{\alpha_i + \alpha_{i+1}}{2}$ represents the average thermal expansion coefficient over the interval.

The summation accounts for the cumulative contribution of all intervals across the entire temperature excursion.
From these calculations, the expansion of copper is found to be **0.277%**.

Regarding the REBCO tapes, unfortunately there is limited data on their high-temperature expansion, as they are not typically used under such conditions. Therefore, the values of its two main components (Hastelloy and copper) were used, applying a force equilibrium similar to that used for the final conductor (equation (10.1)).
For the copper layers, the previously determined values are used, while for Hastelloy, literature data were employed[23]. In this case, the thermal expansion coefficient refers to the relevant temperature range, and interpolation yielded a percentage elongation of 0.186%. Finally, the total elongation of the REBCO tape is calculated as **0.206%**.

Using the values for copper and the REBCO tape, the overall strain of the conductor can be calculated, resulting in **0.273%**.

$\Delta\varepsilon$(%) REBCO	$\Delta\varepsilon$(%) Copper	$\Delta\varepsilon$(%) Conductor	$\Delta\varepsilon$(%) Residual REBCO	$\Delta\varepsilon$(%) Residual Copper
0.206	0.277	0.273	-0.067	0.005

Table 10.1: Thermal expansion during the assembly process. Columns 1 and 2 correspond to the individual conductor components, column 3 to the overall conductor. Columns 4 and 5 show the residual strains in the individual components, with negative values indicating compression.

The residual stresses shown in the table above are obtained from the difference between the expansion of each individual component and the overall expansion of the conductor. As expected, the REBCO tape is in a state of compression at the end of the assembly process, meaning that this correction factor must be applied to the mechanical test results in order to determine the true strain experienced by the REBCO tape.

10.2 Electrical tests at 77K

Similarly to the calculations presented in the previous section, the contraction of the conductor in liquid nitrogen during the electrical tests was evaluated. In this case, the temperature range examined spans from 293K to 77K.

To obtain the contraction data for copper, the software CryoComp was used, which directly provides the strain value based on the material properties and the chosen temperature range. This results in a contraction of **0.303%** for copper.

This time, data on the thermal contraction of the REBCO tape at low temperatures were also available[24], giving a contraction value of **0.22%**.

Applying the force equilibrium from equation (10.1), the overall strain of the conductor is found to be **0.298%** when cooling from room temperature to 77K.

$\Delta\varepsilon$(%) REBCO	$\Delta\varepsilon$(%) Copper	$\Delta\varepsilon$(%) Conductor	$\Delta\varepsilon$(%) Residual REBCO	$\Delta\varepsilon$(%) Residual Copper
0.220	0.303	0.298	-0.078	0.005

Table 10.2: Thermal contraction during electrical tests. Columns 1 and 2 correspond to the individual conductor components, column 3 to the overall conductor. Columns 4 and 5 show the residual strains in the individual components, with negative values indicating compression.

Again, the REBCO tape is in compression within the conductor due to the greater contraction of copper. This must be considered in the final analysis of the tape elongation.

10.3 Correction of test results

The values obtained from the previous calculations were used to correct the tensile test graphs, allowing comparison between the overall conductor strain and that of the REBCO tapes embedded within it.

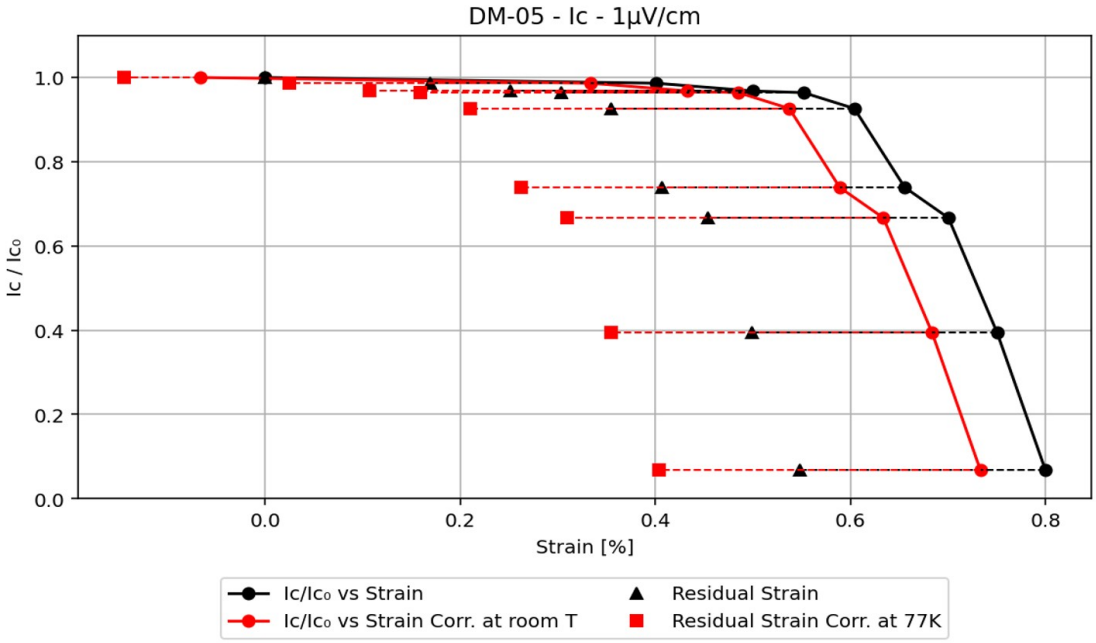

Figure 10.1: Thermal effect correction applied to DM-05 tensile test results.

As shown in the figure above, the corrected data (red) for the REBCO tape are shifted to the left relative to the conductor behavior (black).
In particular, the red circles are offset from the black circles by 0.007%, corresponding to the assembly process. Only this correction factor is applied here, as the maximum strain values during the tensile test at room temperature are being corrected. Since the load is not maintained during electrical tests, the conductor is not affected by contraction due to immersion in liquid nitrogen during this phase.

A different situation occurs for the red squares, which account for both thermal stresses from assembly and those from cooling to 77K for electrical tests, shifting the values further to the left.

It is important to note that this correction does not represent the behavior of the conductor, which is always indicated by the black data, but rather provides an estimate of the actual strains experienced by the REBCO tape.
If an individual tape is subjected to a tensile test, it will be possible to verify whether its characteristics match the developed model. This analysis therefore provides a starting point for comparing the behavior of individual tapes or conductors produced using different assembly techniques.

Chapter 11

Conclusion

11.1 Results Overview

The previous chapters described all the procedures necessary for the assembly and characterization of the conductors. In this section, a summary of the results obtained from these tests is presented.

Conductor Assembly

Among the various procedures performed for conductor assembly, the third method was selected as the definitive one. It requires only a single heat treatment and, through the series connection of the three heating devices, allows obtaining the longest lengths in the shortest time. Furthermore, the guide system adapted to the rolling mill ensures good reproducibility and a uniform distribution of the brazing alloy along the conductor sections.
As shown by the tensile test results, the third method also exhibits the best mechanical properties and the highest critical strain value.
All these features make it undoubtedly the best technique among those examined; therefore, all the mechanical test results presented in this section refer solely to the third assembly process.

Metallography

Some samples obtained from the conductors were subjected to impregnation, polishing, and optical microscopy analysis to evaluate the layer components of the REBCO tape as well as the quality of the brazing achieved through conductor assembly. Further studies will be conducted to establish a correlation between the conductor's structural characteristics and the mechanical test results.

Electrical Tests

Over the course of several months, numerous electrical tests were performed, and procedures were established to ensure reproducible results and to easily identify potential sources of measurement error. The Python code used for data processing was adapted to include functionalities such as pre-calculation of resistances, evaluation of the Ic value based on different critical electric field criteria, and measurement error estimation.
Additional tests were performed to verify current distribution by powering the conductor from one side only instead of both sides, and no changes in the test results were observed.

Tensile Tests

The results from tests with progressively increasing strain revealed a critical strain of approximately 0.6%, corresponding to a stress of around 260 MPa.
Tests involving continuous load-unload cycles did not show any loss in critical current up to a strain of 0.5%.

Compression Tests

The conductor exhibited no performance degradation up to a stress value of 200 MPa.

Bending Tests

Bending tests were conducted with diameters of 150, 120, and 100 mm, and no reduction in critical current was observed. Further tests with smaller diameters will be necessary to determine the critical bending diameter.

Torsion Tests

A degradation of superconducting properties was observed at a twist pitch of 0.9°/mm, with a slower and more gradual decrease in Ic compared to tensile and compression tests.

Thermal Expansion

11.2 Future perspectives

The work carried out during this internship has laid a solid foundation for completing the characterization of the conductor. However, there are still many challenges

to face and goals to achieve for the R&D Conductor group.

Further mechanical characterization will be required through new tests to verify the reproducibility of the results, as well as to complete the ongoing studies, such as the bending tests.

It could also be beneficial to design experimental setups capable of testing the mechanical properties of the conductor directly in liquid nitrogen. This would allow for determining not only the irreversible critical strain but also the reversible one, providing a more comprehensive understanding of the conductor's mechanical behavior.

The conductor will be further investigated through metallographic analysis of selected samples, in order to identify possible correlations between the measured properties and the microstructure. This will also make it possible to assess whether the brazing process ensures consistent results in terms of plate alignment and the thickness of the tin–lead layer.

The assembly process may be revisited by modifying either the assembly technique or the brazing alloy. Nevertheless, the greatest challenge remains the development and optimization of a continuous assembly line capable of producing long conductor lengths.

A prototype of such a system is currently under development. It allows multiple tapes, kept under controlled tension by spools, to pass through a heating device similar to those described in the assembly section. As the tapes travel through the heating zone, the brazing alloy is applied and melted, enabling continuous joining of the layers. The assembled conductor is then cooled in the exit section and automatically wound onto a spool, resulting in a fully continuous production process.

Further improvements can also be implemented in the electrical tests, particularly in the signal filtering stage and in enhancing the accuracy of the measurements.

Finally, a finite element modeling study is also planned, aimed at analyzing the behavior of the composite conductor through a homogenization process. This will allow for a direct comparison between the experimental results and the numerical simulation, providing a deeper understanding of the conductor's mechanical behavior.

Bibliography

[1] *CEA: IRFU*. URL: https://irfu.cea.fr/Phocea/Vie_des_labos/Ast/index.php. (Accessed on: 11/04/2025) (cit. on p. 1).

[2] *National research programme High-temperature superconductors and fusion (PEPR SupraFusion)*. (Accessed on: 28/08/2025). URL: https://www.cnrs.fr/en/pepr/high-temperature-supraconductors-fusion-suprafusion#:~:text=Their%5C%20ability%5C%20to%5C%20generate%5C%20magnetic,fusion%5C%20electricity%5C%20by%5C%20several%5C%20decades. (cit. on p. 1).

[3] *CEA: Suprafusion*. URL: https://www.cea.fr/drf/Pages/Actualites/Vie-de-la-DRF/2023/suprafusion-PEPR-exploratoire-CEA-CNRS.aspx. (Accessed on: 11/04/2025) (cit. on p. 3).

[4] Walid ABDEL MAKSOUD. *Présentation PC4 [SF-DEMO] Démonstrateur de grande envergure*. Internal source, CEA IRFU (Accessed on: 18/08/2025). 2025 (cit. on p. 4).

[5] Nikolay BYKOVSKIY. *HTS high current cable for fusion application*. Accessed on: 15/05/2025. 2017. URL: https://www.researchgate.net/publication/320629393_HTS_high_current_cable_for_fusion_application (cit. on pp. 5, 6).

[6] Carmine Senatore. *Progress in REBCO Conductor Technologies for Ultra-High Field Applications*. Internal source, CEA IRFU (Accessed on: 18/08/2025). 2025 (cit. on p. 6).

[7] Eric Nardon. *Centrale électrique à fusion compacte basée sur les supraconducteurs haute température*. Internal source, CEA IRFU(Accessed on: 11/04/2025). 2025 (cit. on p. 6).

[8] *Critical current densities comparation*. URL: https://www.researchgate.net/figure/Critical-current-densities-for-representative-state-of-the-art-conductors-used-for_fig1_236627864. (Accessed on: 14/04/2025) (cit. on p. 7).

[9] Rui Kang. *Detecting quench in HTS magnets with LTS wires — a theoretical and numerical analysis*. (Accessed on: 14/07/2025). URL: https://arxiv.org/pdf/2109.03982#:~:text=As%5C%20the%5C%20name%5C%20indicates%5C%2C%5C%20HTS,from%5C%20%5C%5B3%5C%E2%5C%80%5C%937%5C%5D. (cit. on pp. 7, 8).

[10] CNRS Xavier CHAUD. *Rubans Supraconducteurs à haute température critique (SHT), champ magnétique intense, fort courant*. Internal source, CEA IRFU (Accessed on: 11/04/2025). 2025 (cit. on p. 9).

[11] J. Gao, X. Wang, Y. Liu, and Z. Chen. *Enhanced adhesion of Ag thin films on Mo substrates using ion beam assisted deposition*. Accessed on: 15/05/2025. 2018. URL: https://www.mdpi.com/1996-1944/11/5/762 (cit. on p. 10).

[12] D. B. Chrisey and G. K. Hubler. *Pulsed laser deposition of thin films: Physics and applications*. Accessed on: 15/05/2025. 2004. URL: https://www.sciencedirect.com/science/article/abs/pii/S0169433203007889 (cit. on p. 11).

[13] E. F. Talantsev. *On the Fundamental Definition of Critical Current in Superconductors*. Accessed on: 05/08/2025. 2017. URL: https://www.researchgate.net/publication/318670891_On_the_fundamental_definition_of_critical_current_in_superconductors (cit. on p. 28).

[14] G. De Marzi. *On the mechanisms governing the critical current reduction in Nb3Sn Rutherford cables under transverse stress*. Accessed on: 05/08/2025. 2021. URL: https://cds.cern.ch/record/2764906/files/s41598-021-86563-x.pdf (cit. on p. 28).

[15] J. W. Ekin. *Offset criterion for determining superconductor critical current*. Accessed on: 05/08/2025. 1989. URL: https://tsapps.nist.gov/publication/get_pdf.cfm?pub_id=30626 (cit. on p. 28).

[16] J. W. Ekin. *Experimental Techniques for Low-Temperature Measurements*. ISBN: 9780195093249. New York: Oxford University Press, 1995 (cit. on pp. 28, 30, 31, 33, 34).

[17] G. Anniballi. *REBCO tape mechanical loading tests and Ic*. Internal source, CEA IRFU (Accessed on: 18/08/2025). 2025 (cit. on p. 57).

[18] Songzhen Yuan. *Electromechanical characteristic of stacked REBCO tapes under tension deformation*. (Accessed on: 14/04/2025). 2023. URL: https://www.sciencedirect.com/science/article/pii/S0011227523001480 (cit. on p. 58).

[19] *Experiments and FE modeling of stress–strain state in ReBCO tape under tensile, torsional and transverse load.* (Accessed on: 09/10/2025). URL: https://iopscience.iop.org/article/10.1088/0953-2048/28/5/055006/pdf (cit. on pp. 75, 76, 89).

[20] *Bending and uniaxial tensile strain effects on the critical current of REBCO coated conductor tapes.* (Accessed on: 09/10/2025). URL: https://www.sciencedirect.com/science/article/pii/S0011227521000436 (cit. on pp. 83, 84).

[21] *Electromechanical degradation of REBCO coated conductor tapes under combined tension and torsion loading.* (Accessed on: 09/10/2025). URL: https://www.sciencedirect.com/science/article/pii/S0020740322002119 (cit. on pp. 88, 89).

[22] *Thermal Expansion of Copper.* (Accessed on: 13/10/2025). URL: https://www.researchgate.net/profile/Robert-Reeber/publication/235924895_Thermal_Expansion_of_Copper/links/59e2ec2a458515393d59f7be/Thermal-Expansion-of-Copper.pdf (cit. on p. 96).

[23] *HASTELLOY C-276 TECHNICAL DATA.* (Accessed on: 13/10/2025). URL: https://www.hightempmetals.com/techdata/hitempHastC276data.php (cit. on p. 97).

[24] Kyle J. Radcliff, Robert P. Walsh, and Robert P. Reed. *The low temperature thermal expansion of materials used for superconducting magnets.* Accessed: 2025-10-13. 2019. URL: https://indico.cern.ch/event/760666/contributions/3391069/attachments/1885053/3107003/M2Or1C-08The_low_temperature_thermal_expansion_of_materials_used.pdf (cit. on p. 98).

Ringraziamenti

Vorrei esprimere la mia gratitudine alla mia relatrice, la professoressa Monica Ferraris, per la disponibilità, la guida attenta e i preziosi suggerimenti che mi ha fornito nel corso di questi mesi. I suoi suggerimenti e il suo supporto hanno rappresentato un valido contributo nello sviluppo di questo lavoro.

Un grand merci à toute l'équipe du CEA avec laquelle j'ai eu le plaisir de travailler durant questi mois.
Merci à Emeric et Gilles pour la confiance que vous m'avez accordée, pour m'avoir offert cette belle opportunité et pour m'avoir guidé avec patience et bienveillance. J'ai beaucoup appris grâce à vous et je suis très reconnaissant pour votre soutien et votre disponibilité au quotidien.
Je tiens également à remercier tous les membres du projet Suprafusion pour votre aide, votre esprit de collaboration et vos conseils toujours précieux. Je vous souhaite sincèrement le meilleur pour la suite du projet et beaucoup de succès dans vos futures réalisations.

Il lavoro svolto per questa tesi ha rappresentato una significativa occasione di crescita, personale e professionale. Spero possa essere solo l'inizio di un percorso ricco di soddisfazioni e nuove sfide.